Euler-Euler / RANS Modeling of Solid-liquid Flow in Stirred Tanks: a Comprehensive Model Validation

Shi, P.; Sommer, A.-E.; Rox, H.; Eckert, K.; Rzehak, R.;

Originally published:

June 2022

Minerals Engineering 185(2022), 107679

DOI: https://doi.org/10.1016/j.mineng.2022.107679

Euler-Euler / RANS Modeling of Solid-liquid Flow in Stirred Tanks: a Comprehensive Model Validation

Pengyu Shi[1*], Anna-Elisabeth Sommer[1], Hannes Rox[1], Kerstin Eckert[1, 2], Roland Rzehak[1]

[1] Helmholtz-Zentrum Dresden – Rossendorf, Institute of Fluid Dynamics, Bautzner Landstrasse 400, D-01328 Dresden, Germany

[2] Technische Universität Dresden, Institute of Process Engineering and Environmental Technology, D-01062 Dresden, Germany

Abstract

Simulations of solid-liquid flow on industrial scales are feasible within the Euler-Euler / RANS approach. The reliability of this approach depends largely on the closure models applied to describe the unresolved phenomena at the particle scale, in particular the interfacial forces. In this work, a set of closure models assembled previously for this kind of application (Shi and Rzehak 2020) is further validated by comparing the predictions to a recent experiment on stirred-tank flows (Sommer et al. 2021), which focuses on dilute suspensions. The dataset used for validation comprises 14 different experimental cases, covering a wide range of particle slip Reynolds number, impeller Reynolds number, and particle Stokes number. For each case, simulation results on the solid velocity and volume fraction as well as liquid velocity and turbulence are compared with the experimental data. It turns out that by and large the experimental data are reasonably well reproduced. However, the measurements show a small but clear effect of modulation of the liquid phase turbulence by the particles. Therefore, several particle-induced turbulence (PIT) models based on the available literature are assessed as well. Our results indicate a reduction in the predicted fluctuations by all PIT models, which improves the results in cases with turbulence suppression but deteriorates those with turbulence augmentation.

Keywords: stirred tanks, solid-liquid flow, Euler-Euler two-fluid model, Reynolds-stress turbulence model, particle-induced turbulence

[*] Corresponding author email: p.shi@hzdr.de

1 INTRODUCTION

Stirred tank reactors are widely used in the minerals industry to maintain solids suspension in continuous hydrometallurgical processes, such as leaching, oxidation, precipitation, neutralization and storage (Wu et al. 2015). For most of these operations, the process performance depends largely on the homogeneity of the suspension, which in turn depends on the fluid and solid dynamics, in particular the turbulence in the liquid phase. Moreover, understanding the two-phase dynamics in solid-liquid stirred tanks and providing validated models are the preconditions for the modeling of three phase (gas-solid-liquid) flow in flotation, which is a critical unit operation used to concentrate valuable minerals in many mineral processing operations (Schwarz et al. 2019, Mesa and Brito-Parada 2019). Therefore, quite a few research works on the dynamic behavior of solid-liquid suspensions have been conducted in the past as reviewed in Mishra and Ein-Mozaffari (2020).

Computational fluid dynamics (CFD) simulations of solid-liquid two-phase flow in stirred tanks are feasible within the Eulerian two-fluid framework of interpenetrating continua. However, accurate numerical predictions rely on suitable closure models describing unresolved phenomena, in particular the interfacial forces. As shown by the comprehensive literature review in Shi and Rzehak (2020), a large number of works exist, in each of which largely a different and often incomplete set of closure relations is compared to a different set of experimental data. For the limited range of conditions to which each model variant is applied, reasonable agreement with the data is mostly obtained, but due to a lack of comparability between the individual works no complete, reliable, and robust formulation has emerged so far. Moreover, usually a number of empirical parameters are involved and have been adjusted to match the particular data, which deteriorates the model's applicability.

To make a first step towards a predictive model, we consider dilute suspensions ($0.01\% < \alpha_S \leq 0.1\%$) where two-way coupling between the phases is necessary (Elghobashi 2006). Apart from interest in its own right, results obtained for this restricted problem also provide a good starting point for the investigation of more complex situations including flows with moderate to high solids loading (Derksen 2018), heat and mass transport (Lu et al. 2019), or gas-solid-liquid three-phase flows (Kim and Kang 1997).

Aspects requiring closure for the system under consideration are: (i) the momentum exchange between the two phases, and (ii) the modulation of the turbulence of the liquid carrier phase by the particles.

Regarding the first aspect, suitable closure relations therefor have previously been collected into a baseline model that serves as a starting point for the simulation of such systems (Shi and Rzehak 2020). There, in addition to the baseline model which takes the full set of closure models (i.e. drag, lift, virtual mass, and turbulent dispersion force) into consideration, seven reduced model variants (summarized in Table 8 of Shi and Rzehak 2020) that originate from different combinations of interfacial force correlations were considered to highlight the importance of various aspects. The predictions were compared with the experimental data from Nouri and Whitelaw (1992), Montante et al. (2012), and Tamburini et al. (2013) and the large-eddy-simulation results from Guha et al. (2008). In most of these works inhomogeneous suspensions have been considered. According to the comparisons, no simplifications were found to be possible in general. More specifically, 1) often the agreement with the validation data deteriorates when using reduced models; 2) the choice of models variants strongly affects the predictions for the solid fraction but only weakly affects those for the mean and fluctuation velocities.

Expanding the range of validity of the baseline model is the major aim of this study, since only a limited range of parameters was covered by the then available data used in Shi and Rzehak (2020). In addition, none of these datasets comprised a full set of observables including solid velocity and volume fraction as well as liquid velocity and turbulence. The recent experiment of Sommer et al. (2021) provides all of these quantities at conditions with varying particle size, particle-to-liquid density ratio, mean solid volume fraction, and impeller rotation speed. These new experimental data now allow to conduct a more systematic validation of the closure models in the present work.

As for the second aspect, the liquid turbulence can be either suppressed or enhanced depending on the detailed flow conditions. Possible mechanisms causing turbulence suppression comprise (Eaton 2009; Balachandar and Eaton 2010) (*a*) the enhanced inertia of the particle-laden flow, (*b*) the enhanced effective viscosity of the particle-laden fluid, and (*c*) the increased dissipation arising from particle drag. On the other hand, particles may also enhance the turbulence via the two mechanisms: (*d*) the enhanced velocity fluctuation due to wake dynamics and (*e*) buoyancy-induced instabilities due to density variation arising from preferential particle concentration. In practice, enhancement and suppression take place simultaneously and the overall modulation depends on the relative strength of the different mechanisms (Elghobashi and Truesdell 1993; Druzhinin and Elghobashi 1999; Balachandar and Eaton 2010, Mathai et al. 2020).

Different criteria to distinguish the enhancement or the suppression effects have appeared in the past. The probably most widely known one originates from Gore and Crowe (1989), according to which particles suppress (enhance) the liquid turbulence when the particle size is smaller (larger) than the characteristic size of large eddies. This classification does not comprise the effects of changing particle material density, nor does it capture the effects of other important parameters such as the Stokes number (Eaton and Fessler 1994; Ferrante and Elghobashi 2003), which relates to mechanisms (*c*) and (*e*), or the particle Reynolds number (Hetsroni 1989; Hoque et al. 2016), which relates to mechanisms (*c*) and (*d*). Recent efforts have sought new criteria to collapse turbulence modulation data. New dimensionless parameters e.g. Stokes load (Poelma et al. 2007) and particle momentum number (Tanaka and Eaton 2008) have therefore been proposed based on more rigorous physical arguments. Nevertheless, a comprehensive assessment carried out by Gai et al. (2020) has indicated that the turbulence modulation cannot be fully characterized by a single parameter. Hence, a reliable model is still not available even for highly simplified situations, e.g. for particles in homogeneous and isotropic turbulence (Meyer 2012, Gai et al. 2020).

Previous E-E simulations of particle-laden stirred-tank flows have therefore either neglected the effect all together or employed highly simplified phenomenological models (see the review in Shi and Rzehak 2020). These models are generally based on two different approaches. The first originates from Sato et al (1981) and treats the particle effects as an additional term in the effective liquid viscosity. Obviously, this approach always predicts an increase in turbulent viscosity (Ochieng and Onyango 2008, Murthy et al. 2008, Qi et al. 2013). The second approach is to add source terms directly to the generation terms in the turbulence model equations following Kataoka et al. (1992). Since both the turbulent kinetic energy and dissipation (or other equivalent parameters e.g. eddy frequency) are modified, this approach can in principle both increase or decrease the turbulent viscosity. Prior work applying this approach may be found in Wang et al. (2003), Shan et al. (2008), and Feng et al. (2012). The performance of these two different approaches has not yet been assessed systematically for particle-laden flows, but they have been verified extensively in bubbly flow simulations (see Rzehak and Krepper (2013) for a review).

That the turbulence modulation by rigid particles and by bubbles can be modeled in an analogous way is not surprising. In particular, it has been shown in the experiments summarized by Gore and Crowe (1989) and newer ones conducted by Hosokawa and Tomiyama (2004) that the turbulence modulation may be described in a unified manner irrespective of the nature of the disperse phase. This similar behavior may be understood by the following two mechanisms. For relatively large particles the wake dynamics is known to be governed by many-body interactions, which act similarly for solid spheres and bubbles (Risso 2008). On the other hand, for small-but-finite-size particles, the modulation of the spectra of both the turbulent kinetic energy and the dissipation has been shown (Yeo et al. 2010) to be closely correlated with the size of the particles but not their inertia. Recent works (Santarelli and Fröhlich 2015, 2016; Yu et al. 2021, Xia et al. 2021) have highlighted the anisotropic nature of the turbulence modulation. Advanced models accounting for this effect have already been proposed for bubbly flows (Colombo and Fairweather 2015; Parekh and Rzehak 2018; Ma et al. 2020), in combination with RSM turbulence models. The applicability of such advanced PIT models, as well as those based on the two common approaches above, will be assessed here for particle-laden flow in stirred tanks.

The remainder of the paper proceeds as follows. In the next section, the E-E /RANS approach together with all investigated PIT models are summarized. Full details of the baseline model from (Shi and Rzehak 2020) are provided for convenience in the Supplementary Material. In section 3, first the selected test cases from the experiment of Sommer et al. (2021) and the numerical setup are outlined, details of the latter being relegated to the Supplementary Material. Then, the simulation results are discussed considering first a base case and then the effect of parametric variations. Lastly an assessment of different PIT model is given. A final summary and conclusions are provided in section 4.

2 OVERVIEW OF MODELS

This section summarizes the models used in the present work. Section 2.1 introduces the conservation equations of the E-E framework and the model used in modeling the turbulence in the liquid phase. The various models on the particle-induced turbulence are described in section 2.2.

2.1 Euler-Euler / RANS approach

The conservation of mass in the solid and liquid phases is governed by the continuity equation

$$\frac{\partial}{\partial t}(\alpha_k \rho_k) + \nabla \cdot (\alpha_k \rho_k \boldsymbol{u}_k) = 0 \tag{1}$$

with the index $k = L, S$ denoting the liquid and solid phases, respectively. In Eq. (1), α is the volume fraction, ρ denotes the density, $\boldsymbol{u}$ is the phase-weighted mean velocity (Drew and Passman, 2006).

The motion of the two phases is governed by the Naiver-Stokes equation, which, in the E-E framework, takes the form

$$\begin{aligned} &\frac{\partial}{\partial t}(\alpha_k \rho_k \boldsymbol{u}_k) + \nabla \cdot (\alpha_k \rho_k \boldsymbol{u}_k \otimes \boldsymbol{u}_k) = \\ &-\alpha_k \nabla p_k + \nabla \cdot \left(2\alpha_k\, \mu_k^{\mathrm{mol}} \mathbf{D}_k\right) - \nabla \cdot (\alpha_k \rho_k \mathbf{R}_k) + \boldsymbol{F}_k^{\mathrm{body}} + \boldsymbol{F}_k^{\mathrm{inter}}. \end{aligned} \tag{2}$$

Here p denotes the pressure, $\mathbf{D} = (\nabla \boldsymbol{u} + (\nabla \boldsymbol{u})^{\boldsymbol{T}})/2$ is the strain rate tensor, and μ^{mol} is the molecular dynamic viscosity. Following previous numerical work, μ_S^{mol} is assumed to be identical with μ_L^{mol}.

The body forces $\boldsymbol{F}_k^{\text{body}}$ comprise the gravity force as well as centrifugal and Coriolis forces where a rotating frame of reference is adopted. The term $\boldsymbol{F}_k^{\text{inter}}$ accounts for the momentum transfer between the phases. Due to momentum conservation the relation $\boldsymbol{F}_S^{\text{inter}} = -\boldsymbol{F}_L^{\text{inter}}$ holds. This term comprises of a number of contributions and the corresponding models employed here are summarized in Table 1. A detailed discussion thereof is given in section A of the Supplementary Material.

Table 1: Summary of particle force correlations based on two-way coupling.

force	**reference**
drag	Schiller and Naumann (1933) modified for turbulence effects as in Shi and Rzehak (2020)
lift	Shi and Rzehak (2019)
turbulent dispersion	Lopez de Bertodano (1998) with turbulence time scales from Shi and Rzehak (2020)
virtual mass	constant coefficient $C_{\text{VM}} = 1/2$

In Eq. (2), $\mathbf{R}$ is the Reynolds stress tensor and is defined in terms of the turbulent fluctuating velocities $\boldsymbol{u}'_k$ as $\mathbf{R}_k = \langle \boldsymbol{u}'_k \otimes \boldsymbol{u}'_k \rangle$, where $\langle \quad \rangle$ corresponds to ensemble averaging. $\mathbf{R}_L$ is obtained by directly solving a transport equation as discussed in the following, while $\mathbf{R}_S$ is presently neglected. The index 'L' is then dropped throughout this section for notational convenience. The transport equation for the Reynolds stress tensor $\mathbf{R} = \langle \boldsymbol{u}' \otimes \boldsymbol{u}' \rangle$ is given as

$$\begin{aligned} \frac{\partial}{\partial t}(\alpha\rho\mathbf{R}) + \nabla\cdot(\alpha\rho\boldsymbol{u}\otimes\mathbf{R}) = {} & \nabla\cdot\left(\alpha\left(\boldsymbol{\mu}^{\text{mol}} + C_s\boldsymbol{\mu}^{\text{turb}}\right)\nabla\otimes\mathbf{R}\right) \\ & + \alpha\rho\left(\mathbf{P} + \boldsymbol{\phi} - \frac{2}{3}\varepsilon\mathbf{I} + \mathbf{G}\right) + \mathbf{S}^R, \end{aligned} \tag{3}$$

and that for the isotropic turbulent dissipation rate ε as

$$\begin{aligned} \frac{\partial}{\partial t}(\alpha\rho\varepsilon) + \nabla\cdot(\alpha\rho\boldsymbol{u}\varepsilon) = {} & \nabla\cdot\left(\alpha\left(\boldsymbol{\mu}^{\text{mol}} + C_\varepsilon\boldsymbol{\mu}^{\text{turb}}\right)\cdot\nabla\varepsilon\right) \\ & + \alpha\rho\frac{\varepsilon}{k}\left(C_{\varepsilon,1}\frac{1}{2}tr(\mathbf{P}) - C_{\epsilon,2}\varepsilon\right) + S^\varepsilon. \end{aligned} \tag{4}$$

Individual terms appearing on the right side of equation (3) describe diffusion, production, pressure-strain correlation, dissipation, and generation due to body forces (here frame rotation). The last term in Eqs. (3) and (4), i.e. $\mathbf{S}^R$ and S^ε, are the PIT source terms and will be described in section 2.2. The SSG RSM turbulence model proposed by Speziale, Sarkar, and Gatski (1991) is applied. A detailed description on the concept of this model as well as a summary on the values of the pertinent coefficients used in the present work can be found in Shi and Rzehak (2020).

2.2 Models for the particle-induced turbulence

In addition to the shear-induced turbulence discussed above, the presence of the particles induces additional disturbances to the ambient flow, which can either enhance or attenuate the turbulence depending on the flow condition. This turbulence modulation, also referred to as particle-induced turbulence (PIT), needs to be modeled. In this context, a simple approach is to just add an extra particle-induced contribution to the effective viscosity following Sato et al (1981, hereafter termed Sato-PIT). Since the shear-induced turbulence here is modeled without referring to a turbulent viscosity, this approach is implemented by replacing the molecular viscosity of the liquid phase, μ_L^{mol}, in the momentum equation (2) by an effective viscosity

$$\mu_L^{\mathrm{eff}} = \mu^{\mathrm{mol}} + \mu^{\mathrm{PIT}}, \tag{5}$$

where μ^{PIT} is the particle-induced contribution. Following Sato et al (1981), μ^{PIT} is modeled as

$$\mu^{\mathrm{PIT}} = C_{\mathrm{p}} \rho_L \alpha_S d_{\mathrm{p}} u_{\mathrm{rel}}, \tag{6}$$

where in accordance with previous works (Ochieng and Onyango 2008, Murthy et al. 2008, Qi et al. 2013) $C_{\mathrm{p}} = 0.6$ is applied.

An alternative approach is to add source terms directly to the generation terms in the turbulence model equations following Kataoka et al. (1992). This approach may be implemented by expressing the source terms $\mathbf{S}^R$ and S^ε in Eqs. (3) & (4) as

$$\mathbf{S}^R = S^k \left(a[\hat{\boldsymbol{u}}_{\mathrm{rel}} \otimes \hat{\boldsymbol{u}}_{\mathrm{rel}}] + \frac{1}{2}(2-a)[\mathbf{I} - \hat{\boldsymbol{u}}_{\mathrm{rel}} \otimes \hat{\boldsymbol{u}}_{\mathrm{rel}}] \right) \tag{7}$$

and

$$S^\varepsilon = C_{\varepsilon \mathrm{P}} \frac{S^k}{\tau}, \tag{8}$$

where S^k is proportional to the work due to the drag force, i.e.

$$S^k = C_{k\mathrm{P}} \boldsymbol{F}_L^{\mathrm{drag}} \cdot \boldsymbol{u}_{\mathrm{rel}}. \tag{9}$$

In Eq. (7), $\mathbf{I}$ is the identity matrix, $\hat{\boldsymbol{u}}_{\mathrm{rel}}$ is a normalized vector in the direction of the relative velocity between the two phases, i.e. $\hat{\boldsymbol{u}}_{\mathrm{rel}} = \boldsymbol{u}_{\mathrm{rel}}/u_{\mathrm{rel}}$. The two terms in the bracket of Eq. (7) correspond to the longitudinal and the transverse components of the contribution to the liquid Reynolds stress by the dispersed phase and the coefficient a governs their ratio.

The PIT model following this approach can assume two different forms depending on the value of the coefficient a appearing in Eq. (7). Assuming this contribution to be isotropic yields $a = 2/3$, which recovers the PIT model applied in prior works employing the isotropic two-equation turbulence models (e.g. Wang et al. 2003, Shan et al. 2008, and Feng et al. 2012). In these previous works the empirical coefficients $C_{\varepsilon \mathrm{P}}$, $C_{k\mathrm{P}}$ appearing in Eqs. (8) and (9) were treated as small constants while the timescale τ in Eq. (8) was assumed to be proportional to k/ε. In the present work, the suggested correlations from Ma et al. (2017) are applied, which give

$$C_{\varepsilon \mathrm{P}} = 0.3 C_{\mathrm{D},0}, \qquad C_{kP} = \min\left(0.18 Re_{\mathrm{p}}^{0.23}, 1\right), \qquad \tau = d_{\mathrm{p}}/u_{\mathrm{rel}}. \tag{10}$$

Hereafter, the PIT model implemented following Eqs. (7)-(10) and $a = 2/3$ will be termed as iso-PIT.

Taking advantage of the SSG RSM model applied in this work, the source term $\mathbf{S}^R$ can also be treated as anisotropic, which is indeed the case observed in both experimental (Geiss et al. 2004, Poelma et al. 2007) and DNS studies (Yu et al. 2021, Xia et al. 2021). Following Ma et al. (2020), a is correlated with the particle Reynolds number via

$$a = \min\left(0.67 + 0.67\exp\left(370Re_{\mathrm{p}}^{-1.2}\right), 2\right). \tag{11}$$

The PIT model implemented following Eqs. (7)-(11) will be termed as aniso-PIT.

The proposal to cast the source term $\mathbf{S}^R$ following Eq. (7) deserves some explanation. First, it has to be pointed out that for flows in simple geometry, e.g. vertical pipe or channel flows, no such complexity is required, as the relative velocity is everywhere unidirectional and independent of position. The need to consider local variations of the direction of relative velocity arises when the flow considered is multi-dimensional, e.g. stirred-tank flows. In this case one has to cast the source term so that it is independent of the choice of coordinate directions. This can be proceed using the idea based on proper Euler angles (see Appendix C of Ma et al. (2020) for the details). After some manipulations, the transformation turns out to follow Eq. (7).

3 RESULTS AND DISCUSSION

The experiment of Sommer et al. (2021) investigated the solid-liquid two-phase flow in a stirred tank of a standard configuration. The tank was cylindrical and had a diameter $D_{\mathrm{t}} = 90$ mm. The liquid fill height H was the same as the tank diameter, i.e. $H = 90$ mm. A standard Rushton turbine with a diameter $D_{\mathrm{i}} = 30$ mm was installed with a separation distance from the tank bottom of $C_{\mathrm{i}} = 30$ mm. The height (axial) and width (radial) of the impeller blades are $H_{\mathrm{bla}} = 6$ mm and $W_{\mathrm{bla}} = 7.5$ mm, respectively. Four baffles were installed on the tank wall every 90°, which extended over the entire tank height and had a width of 9 mm. Other geometric details can be found in Sommer et al. (2021). Deionized water was used as the liquid phase. Two different types of particles were considered, namely Polyethylene spheres (PE) and glass beads (GL) having a density ratio with respect to water of 1.1 and 2.5, respectively. For each type of particles, different operational conditions concerning the impeller rotation speed Ω, the mean solid volume fraction $\bar{\alpha}_{S,\mathrm{ave}}$, and the particle diameter d_{p} were considered in the experiment. 35 datasets comprising spatially resolved data on the solid mean velocity and solid fraction as well as liquid mean velocity and fluctuation are available from this experiment.

In the present work, CFD simulations are performed on 14 out of the 35 experimental cases. As summarized in Table 2, the investigated cases comprise one single-phase case with an impeller rotation speed of $\Omega = 1500$ rpm and two series of cases concerning two-phase flows which are distinguished by the type of the particle. For both the PE and GL series, the "base" case corresponds to the situation with $\Omega = 1500$ rpm, $\bar{\alpha}_{S,\mathrm{ave}} = 0.05\%$, and $d_{\mathrm{p}} = 0.165$ mm. In comparison, "vofS" and "vofL" correspond to cases with smaller and larger solid volume fractions of $\bar{\alpha}_{S,\mathrm{ave}} = 0.025\%$ and 0.1%, respectively. Similarly, cases involving relatively small (resp. large) particles are termed as "dpS" (resp. "dpL"), while those involving very small (resp. only moderate) values of impeller rotation speed are termed as "rpm650" (resp. "rpm1000"). Note that in the GL series the impeller rotation speed is fixed at $\Omega = 1500$ rpm since pronounced sedimentation was observed in the experiment at lower impeller rotation speeds. Finally, a special case "PE-dpS-vofL" is included since the corresponding experiment shows a particularly strong turbulence modulation.

The simulations are performed using ANSYS CFX release 21.1. A detailed discussion of the discretization schemes, the boundary conditions, and the implementation of the multiple-reference-frame approach (MRF) to treat the rotating parts can be found in Shi and Rzehak (2018, 2020). Here a summary is provided in section B of the Supplementary Material. To match the experiment, a special procedure (Deen et al. 2002; Shi and Rzehak 2018) is applied during post processing for the present simulations to obtain the mean and fluctuating velocities in the inner, rotating MRF block. In particular, the axial profile of the mean velocity of both phases at a given radial position r is obtained by averaging all the results over the cylindrical surface defined by r. Details of this procedure are also given in section B of the Supplementary Material.

Table 2: Summary of the investigated cases and the corresponding power numbers predicted by the simulations.

name	Ω (rpm)	ρ_S/ρ_L (-)	$\bar{\alpha}_{S,\mathrm{ave}}$ (%)	d_{p} (mm)	N_{p} (-)
single-phase	1500	-	-	-	3.64
cases concerning PE particles					
PE-base	1500	1.1	0.050	0.165	3.68
PE-vofS	1500	1.1	0.025	0.165	3.71
PE-vofL	1500	1.1	0.100	0.165	3.64
PE-rpm1000	1000	1.1	0.050	0.165	3.63
PE-rpm650	650	1.1	0.050	0.165	3.69
PE-dpS	1500	1.1	0.050	0.067	3.76
PE-dpL	1500	1.1	0.050	0.450	3.72
PE-dpS-vofL	1500	1.1	0.100	0.067	3.83
cases concerning GL particles					
GL-base	1500	2.5	0.050	0.165	3.67
GL-vofS	1500	2.5	0.025	0.165	3.69
GL-vofL	1500	2.5	0.100	0.165	3.69
GL-dpS	1500	2.5	0.050	0.067	3.74
GL-dpL	1500	2.5	0.050	0.425	3.62

The mesh independency of the numerical results is assessed for three fully structured meshes (called mesh 144, mesh 180, and mesh 240) with increasing resolution. The numerical results for the mean and fluctuation velocities as well as the solid distribution are compared with the corresponding experimental results for the case GL-base (see Table 2). Details of the meshes and the comparison are provided in Appendix B. It turns out that to reduce the numerical error the mesh with the highest resolution, i.e. mesh 240, should be applied in principle. However, taking into account the required CPU time as well (see section C of the Supplementary Material), the compromise is made to apply mesh 180 as the default for all further simulations to be presented in this work. Results from mesh 240 will be included in addition where notable deviations between the computational and the experimental results are seen, in order to better reveal their origin.

Before discussing the spatially resolved results from the simulations, first the magnitude of the predicted power number, $N_{\mathrm{p},\Gamma} = 2\pi\Omega\Gamma/\rho_L\Omega^3 D_i^5$ (with Γ denoting the torque acting on the impeller and the shaft) is checked, which is one of the most important and representative global dimensionless parameters for a stirred vessel. The numerical results obtained for each of the investigated cases are summarized in the last column of Table 2. In most of the investigated cases a power number around 3.6 is obtained which is significantly lower than the value of 5 from

Rushton et al. (1950), but in good agreement with the correlation of Bujalski et al. (1986). As already discussed in the experimental work (Sommer et al. 2021), this is most likely due to the relatively larger thickness of the impeller blades. A similar trend was observed in the experiments of Rutherford et al. (1996) and Chapple et al. (2002) and the DNS simulation of Gillissen and Van den Akker (2012).

An alternative approach to estimate the power number is to equate the power input to the total energy dissipate rate. The power number obtained from this approach ($N_{\mathrm{p},\varepsilon}$) is always smaller than that estimated from the torque ($N_{\mathrm{p},\Gamma}$). Moreover, with increasing grid resolution $N_{\mathrm{p},\Gamma}$ experiences only a small variation, while $N_{\mathrm{p},\varepsilon}$ shows a gradual increase and reaches about 80 percent of $N_{\mathrm{p},\Gamma}$ based on the most refined mesh (mesh240) which comprises 13.8 million cells. A similar trend was also reported in Coroneo et al. (2011) using the RANS approach. Moreover, in the DNS study by Gillissen and Van den Akker (2012) $N_{\mathrm{p},\varepsilon}$ is still slightly smaller than $N_{\mathrm{p},\Gamma}$ even using 2.9 billion grid cells. Based on these findings one may tentatively conclude that the underestimated power number from the dissipation is mostly related to the inevitable truncation error, which is more pronounced when a coarser grid is used.

The remainder of this section discusses the simulation results for all cases listed in Table 2. More specifically, section 3.1 provides a comprehensive discussion on the two “base” cases with different types of particles. Section 3.2 outlines the effects of the operational parameters, i.e. the particle size, the mean solid fraction, and the impeller rotation speed. No PIT model has been used in obtaining the simulation results up to this point. To supplement this, section 3.3 presents results obtained by different PIT models with a focus on the three typical cases: PE-base, GL-base, and PE-dpS-vofL.

3.1 Results for base cases

Results for the two base cases are discussed first to get an idea on the particle effects. Here, base case corresponds to the situation with an impeller rotation speed of $\Omega = 1500$ rpm, a mean solid fraction of $\bar{\alpha}_{S,\mathrm{ave}} = 0.05\%$, and a mean particle diameter of $d_{\mathrm{p}} = 0.165$ mm. PE-base corresponds to the base case using PE particles which have a density ratio with respect to the liquid phase of 1.1. Similarly, GL-base corresponds to the case with GL particles with a density ratio of 2.5. Results for the mean velocities, the solid fraction, and the fluctuating velocity of the liquid phase are discussed in the following.

3.1.1 Mean liquid and solid velocities

Figure 1 summarizes the results for the mean liquid velocity obtained at a radial position $2r/D_{\mathrm{t}} = 0.44$ near the tip of the impeller. With the presence of the particles, the experimental data reveal no substantial change in the axial component of liquid velocity, but a notable decrease in the radial component. In particular, in the case with GL particles the peak radial velocity is seen to decrease by about 23% with a solid loading of only 0.05%. A further check on the data of Sommer et al. (2021) indicates that a decrease by 14% already took place even with only 0.025% GL particles. This decrease has also been observed in the recent experiment of Li et al. (2018) (their Fig. 15), but for solid loadings of more than 1%. Compared with the experiment, simulation results show relatively small particle effects on the liquid mean velocities. The agreement is ok far enough below and above the impeller but not around it for both velocity components. This mismatch will be picked up later together with the mean solid velocity.

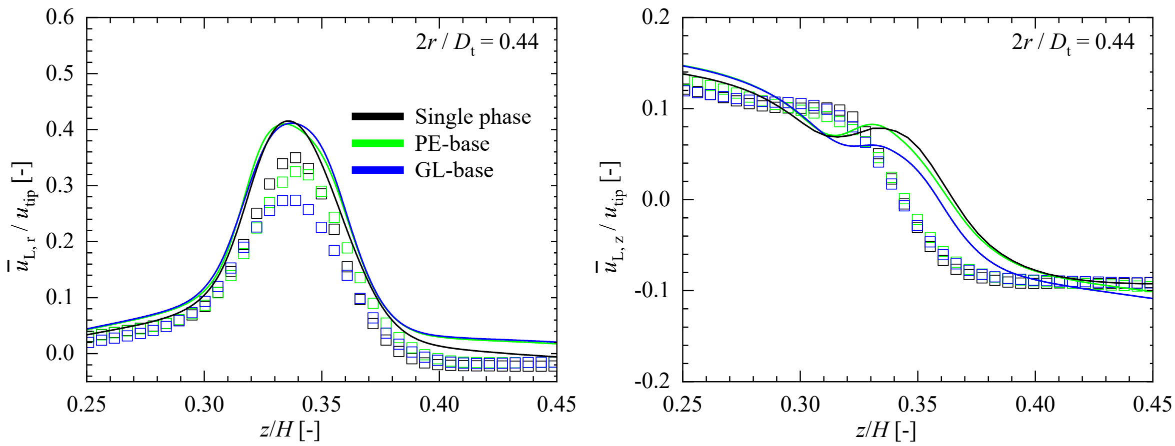

Figure 1. Axial profiles of the radial (left) and axial (right) components of the mean liquid velocity (normalized by the tip velocity of the impeller $u_{\mathrm{tip}} = \pi D_{\mathrm{t}} \Omega / 180$) at a radial position $2r/D_{\mathrm{t}} = 0.44$. Solid lines: simulation results according to the model outlined in Table 1; symbols: experimental data from Sommer et al. (2021).

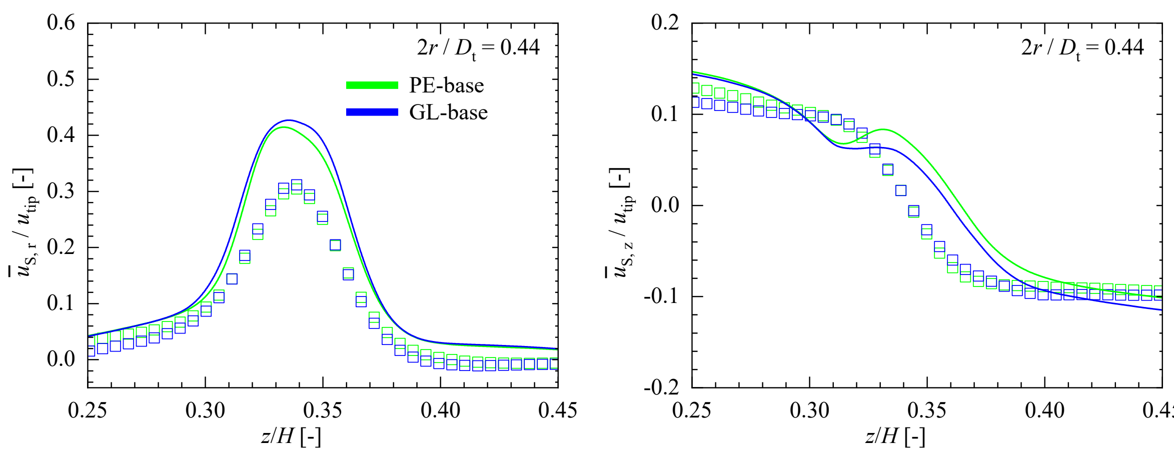

Figure 2. As Figure 1 but for the solid phase: Polyethylene spheres (PE) and glass beads (GL).

Results for the mean solid velocities at the same radial position are shown in Figure 2. Both the experimental and the computational results show only a very small change in the solid velocities with increasing solid density (i.e. from PE-base to GL-base). This vanishingly small difference in the mean solid velocity indicates that for both particle types the inertia are still small. One may therefore expect their motion to mostly follow the mean liquid flow. This can be examined by checking the difference between the results shown in Figure 2 and Figure 1. It turns out that the above expectation applies for all simulation results and for the experimental data concerning PE particles, as the slip velocities revealed from these results are found vanishingly small. The experimental data concerning GL particles, however, indicate that the peak radial solid velocity is about 15% larger than that of the liquid phase. The present simulation is unable to reproduce this sizable slip.

Figure 3 shows the results for the mean solid velocity at a radial position $2r/D_{\mathrm{t}} = 0.75$. Similar to those in Figure 2, the difference between the experimental results obtained for PE and GL particles is negligibly small. Owing to the spreading of the impeller stream, the mean velocity of both phases decreases with increasing radial distance. Compared with Figure 2, experimental results indicate a decrease in the peak of the radial velocity of about 0.05 (normalized by u_{tip}) for both types of particles. This decrease is qualitively captured by the simulations, although the magnitude of the peak values is overestimated at these two radial positions. In comparison, the decrease in the axial component of the mean velocity is more pronounced. At $2r/D_{\mathrm{t}} = 0.44$ the magnitude of the maximum axial velocity in the considered axial range is around 0.1, while it has decreased by a factor of 2 at $2r/D_{\mathrm{t}} = 0.75$. Simulation results reproduce these changes and show quite good agreement with the experimental data.

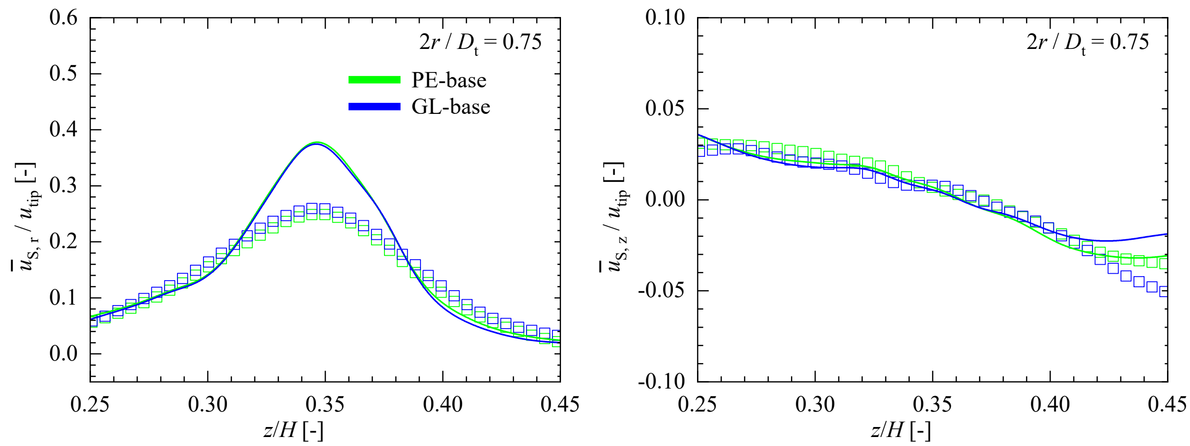

Figure 3. As Figure 1 but for the solid velocity at a radial position $2r/D_{\mathrm{t}} = 0.75$ far away from the impeller.

3.1.2 Solid fraction

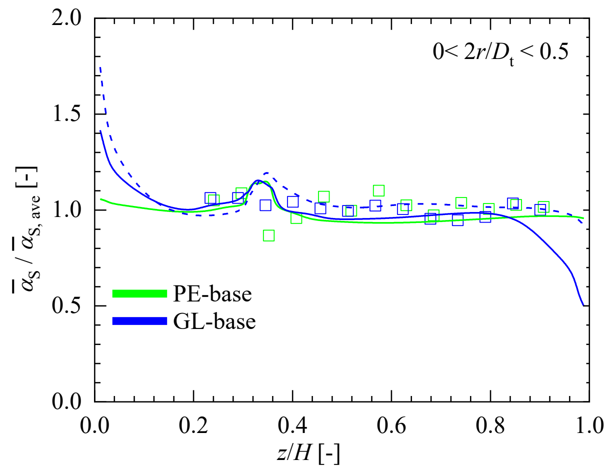

Figure 4. Results for the horizontally averaged solid fraction along the height of the tank. Solid (dashed) lines: present simulation results from mesh 180 (mesh 240); symbols: experimental data from Sommer et al. (2021).

Results for the solid fraction along the height of the tank are shown in Figure 4. At each z/H, $\bar{\alpha}_S$ corresponds to the area-averaged solid fraction in the horizontal plane defined by z/H for $0 < 2r/D_{\mathrm{t}} \leq 0.5$. For both cases, experimental data available for $0.2 < z/H < 0.9$ show no significant variation along the height, indicating the suspension being rather homogenous. Only in the region near the impeller (i.e. at $z/H \approx 0.33$), the solid fraction for PE particles is about 15% lower than the mean value. Simulation results show generally good agreement with the experimental data with two exceptions. One is the region near the tank top where the calculated solid fraction for GL particles decreases with increasing z/H, in contradiction to the experiment. This mismatch is a numerical error caused by the applied mesh (mesh 180, see section B of the Supplementary Material for details), which was chosen for reasons of CPU time despite its somewhat too low resolution, and can be eliminated using the more refined mesh, i.e. mesh 240 (see the dashed line in Figure 4). Interestingly, the result for the PE-base case, which is obtained also using mesh 180, agrees well with the measured data in this region. Not surprisingly this indicates a possible dependency of the required mesh resolution on the particle properties (here, density).

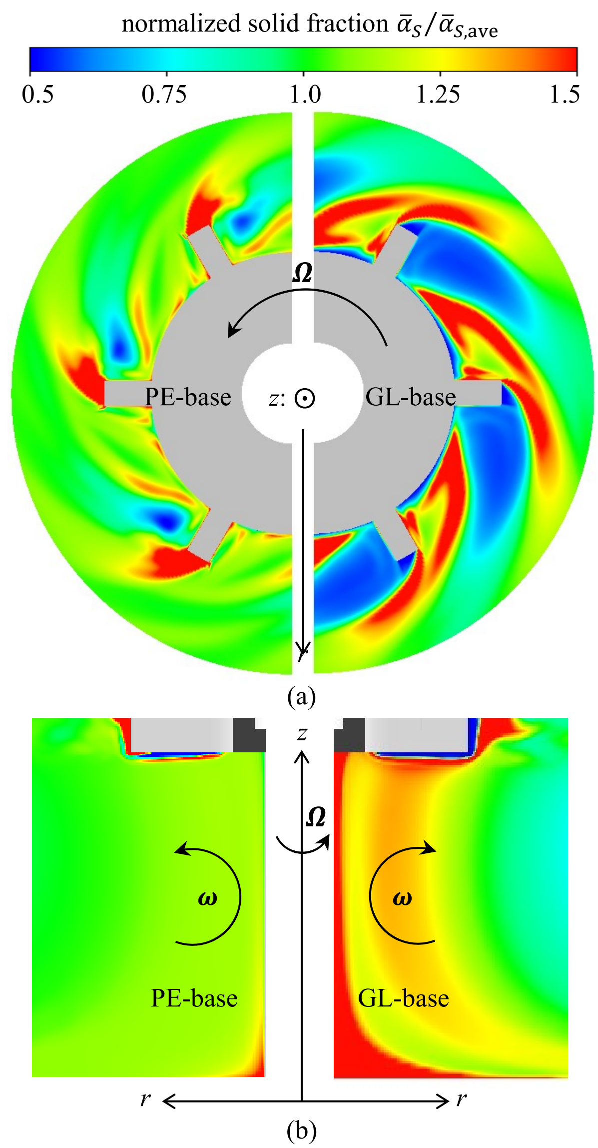

Figure 5. Simulation results for the solid fraction (normalized by $\bar{\alpha}_{S,\mathrm{ave}}$) in (a) the horizontal plane $z/H = 0.33$ (i.e. at the center of the impeller) for $0 < 2r/D_\mathrm{t} \leq 0.5$ and (b) the vertical plane located midway between two baffles for $0 < 2r/D_\mathrm{t} \leq 0.5$ and $0 < z/H \leq 0.4$. In both (a) and (b) the left and right panels correspond to the cases PE-base and GL-base, respectively. The impeller rotation $\boldsymbol{\Omega}$ is along the z axis, i.e. in the anticlockwise direction in (a).

The other and more interesting exception where the simulations results deviate from the experimental data occurs in the region near the impeller. As shown in Figure 4, there the predicted solid fractions are larger than both the mean value $\bar{\alpha}_{S,\mathrm{ave}}$ and the experimental results. To better understand this deviation, the predicted solid fraction in the horizontal plane at the center of the impeller is examined. The results for both particles are shown in Figure 5 (a). It turns out that a large amount of particles accumulates in the vicinity of the impeller tips. Meanwhile, a region with lower-than-average solid fraction exists behind the impeller blades (note that in Figure 5 (a) the impeller rotates along the z axis, i.e. in the anticlockwise direction), which is more pronounced for GL particles. Such a highly non-uniform distribution of particles at the center of the impeller has also been reported in Derksen (2003, Fig. 3), where a highly resolved simulation based on the E-L / LES approach has been conducted. Averaging the values over the horizontal plane gives a higher-than-average solid fraction for both particles, i.e. the higher-concentration region outweighs the lower one.

In Figure 4, the calculated solid fractions for GL and PE particles deviate from each other when approaching the tank bottom (i.e. with z/H decreasing from 0.2 to 0). More specifically, for GL particles the profile sharply increases towards a distinct maximum at the tank bottom, while for PE particles it shows only a small variation reaching a maximum that is only slightly larger than the mean value. These different behaviors may be better understood by checking the solid fraction distribution in the vertical plane midway between two baffles underneath the impeller for $0 < 2r/D_{\mathrm{t}} \leq 0.5$ as shown in Figure 5 (b). These results indicate that in the lower part of the tank PE particles are still rather homogenously suspended, while GL particles accumulate in the tank center especially when approaching the tank bottom.

The latter behavior has also been observed in the highly resolved simulation of Derksen (2003, Fig. 3). The underlying mechanism is outlined in the following. First, it is noted that, when the impeller is initially at rest, both particles would deposit at the bottom, owing to their larger density compared with that of the ambient liquid. Impeller rotation generates two counter rotating vortices in the vertical plane underneath the impeller. Their orientations as characterized by the flow vorticity $\boldsymbol{\omega}$ are illustrated in Figure 5 (b). The associated mean flow carries the accumulated particles at the bottom first to the tank center and then upwards to the impeller. Particle suspension driven by this advection mechanism is certainly more efficient for particles with less inertia, making the distribution of PE particles more homogenous than that of GL particles. Nevertheless, as seen in Figure 5 (b), a high solid fraction is present at the bottom closest to the tank center even for PE particles, owing to the relatively weak mean-flow advection in this region.

3.1.3 Fluctuation of liquid velocity

Figure 6 and Figure 7 summarize the results for the liquid velocity fluctuation at two radial positions of $2r/D_{\mathrm{t}} = 0.44$ and 0.80, respectively. Experimental results indicate that near the impeller at $2r/D_{\mathrm{t}} = 0.44$, the peak of both the radial ($u'_{\mathrm{L,r}}$) and axial ($u'_{\mathrm{L,z}}$) components of fluctuation in the PE-base case are about 10% smaller than their counterparts in the single-phase case. In comparison, the change caused by GL particles is seen to be relatively small. Farther away from the impeller at $2r/D_{\mathrm{t}} = 0.80$, the reduction in the peak caused by PE particles almost vanishes and hardly any difference between the data for the two particle-laden cases can be observed.

Turning to the simulation results, good agreement with the experimental data is achieved in the single-phase case at $2r/D_{\mathrm{t}} = 0.44$, while at $2r/D_{\mathrm{t}} = 0.80$ in particular the axial fluctuation is underestimated by about 30%. Compared to the single-phase case, the presence of both particles tends to suppress the liquid velocity fluctuation at both radial positions in the simulations. This is in qualitative agreement with the experimental observation with the only exception being the radial fluctuation profiles in the GL-base case at $2r/D_\mathrm{t} = 0.44$. There, compared with the single-phase results, the peak value is seen to decrease in the simulation, instead of remaining unchanged as reported in the experiment.

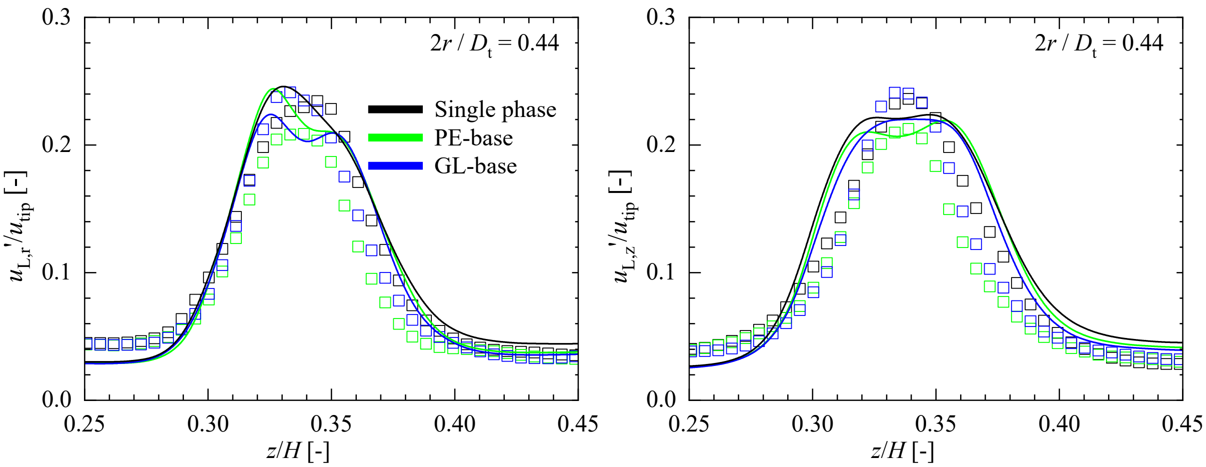

Figure 6. Axial profiles of the radial (left) and axial (right) components of the liquid velocity fluctuation at a radial position $2r/D_\mathrm{t} = 0.44$ close to the impeller. Lines: present simulation results; symbols: experimental data from Sommer et al. (2021).

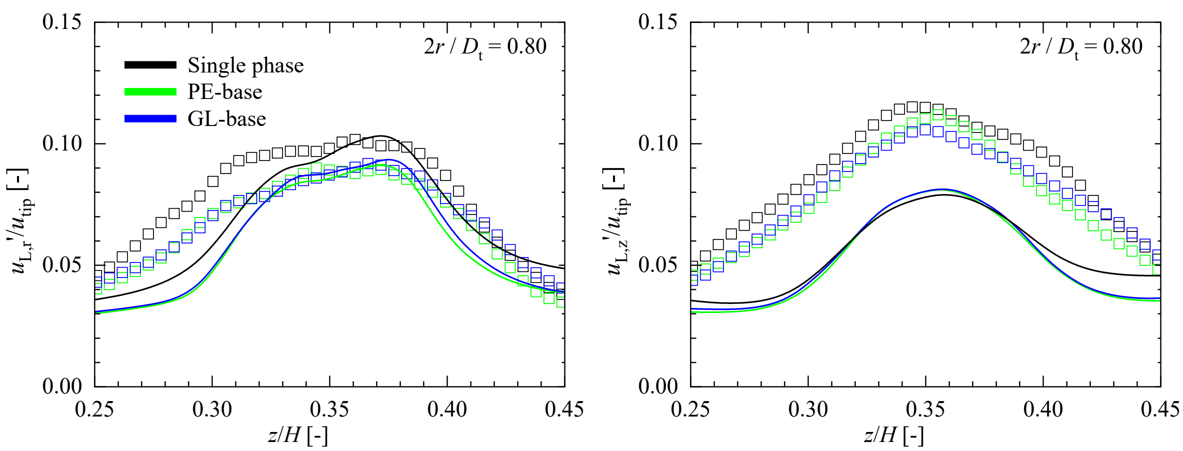

Figure 7. As Figure 6 but at a radial position $2r/D_\mathrm{t} = 0.80$ far away from the impeller.

Since no PIT model is applied in the two-phase simulations the notable variation with respect to the single-phase results is unexpected at first glance. To seek the origin of this variation, the budget of the turbulent kinetic energy $k = R_{ii}/2$ is shown in Figure 8 at two radial positions of $2r/D_\mathrm{t} = 0.44$ and 0.80. For the sake of brevity, results are shown only for the production ($P_{ii}/2$), the dissipation ($-\varepsilon$), and the mean-flow convection ($-\,\mathrm{D}k/\mathrm{D}t$). The variation in the diffusion ($\nabla \cdot \left[\alpha\left(\mu^{\mathrm{mol}} + C_s\mu^{\mathrm{turb}}\right)\nabla k\right]$) can be estimated based on the balance of the budget equation. As seen from the different scales of the two panels, the contributions at $2r/D_\mathrm{t} = 0.44$ are at least an order of magnitude larger than their counterparts at $2r/D_\mathrm{t} = 0.80$.

In the single-phase case, the dissipation and the convection at $2r/D_\mathrm{t} = 0.44$ reach their maximum at approximately $z/H = 0.34$, a position at which the mean radial flow reaches its maximum as well (left panel of Figure 1). Away from the peak, their magnitudes gradually decrease and are nearly symmetric with respect to the position $z/H = 0.34$, a feature that has also been observed in jet flows (Pope 2000, chapter 5). At the same radial position, the production shows a double-peaked profile, featuring a local minimum at $z/H = 0.34$ and two local maxima about $0.02H$ away on each side. Unlike the dissipation and convection, the production is asymmetrically distributed with the lower (upper) part contributing more (less) energetically to the turbulent kinetic energy at $2r/D_\mathrm{t} = 0.44$ (0.80).

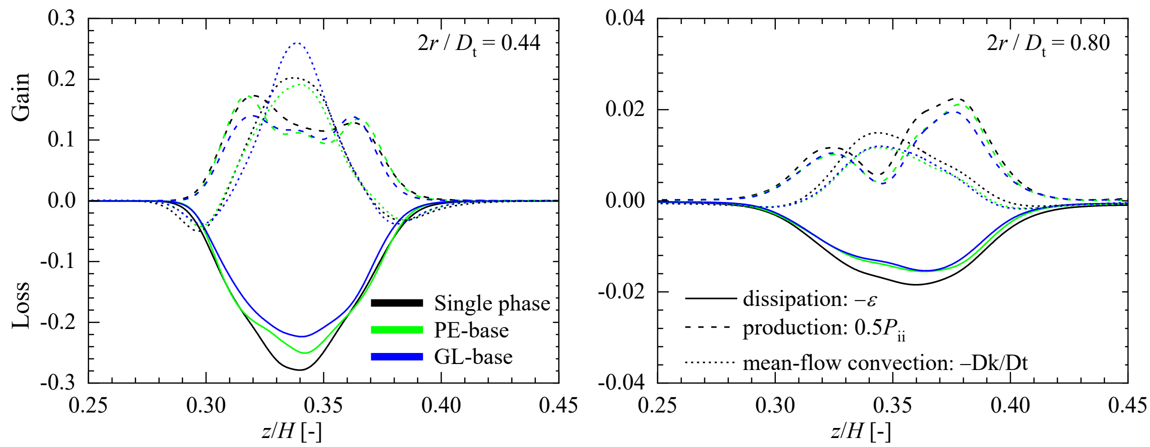

Figure 8. Simulation results for the budget of the turbulent kinetic energy [based on Eq. (3)] at two radial positions of $2r/D_\mathrm{t} = 0.44$ (left) and $2r/D_\mathrm{t} = 0.80$ (right). Results are shown for the three major contributions, i.e. the dissipation, the production, and the mean-flow convection (denoted by different type of lines). All quantities are normalized by $u_\mathrm{tip}^3/D_\mathrm{t}$.

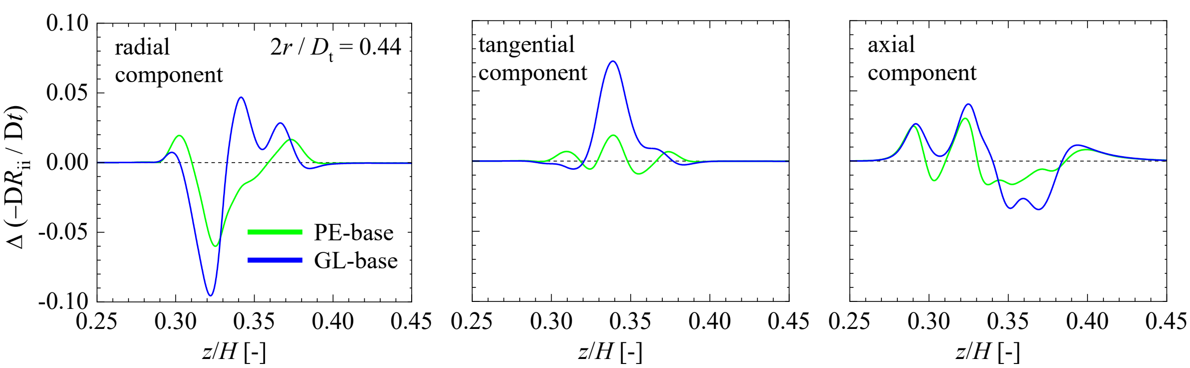

Figure 9. Change in the mean-flow convection of the normal Reynolds stresses caused by the particles.

In the two-phase cases, the shapes of the profiles remain the same, but the predicted dissipation is seen to be smaller than in the single phase case, in agreement with previous experimental observations in particle-laden stirred-tank flows (Unadkat et al. 2009, Gabriele et al. 2011, Chen et al. 2011). The production term also experiences a reduction by both particles, which roughly balances the decrease in dissipation in the case with PE particles. The predicted turbulence modulation can be mostly understood by checking the variation in the convection, which is seen to depend on the position. At $2r/D_\mathrm{t} = 0.44$ (left panel of Figure 8), a slight reduction is seen in the PE-base case, making the predicted fluctuation decrease. Meanwhile, a significant increase in the peak of the convection is seen in the GL-base case.

Closer inspection indicates that the redistribution of this increase is anisotropic. This is revealed in Figure 9, where the difference in the convection of the three normal Reynolds stresses to the single-phase results, i.e. $\Delta\left(-\frac{\mathrm{D}R_{ii}}{\mathrm{D}t}\right)$, is illustrated. It is seen that only the tangential component in the GL-base case (blue line in the middle panel of Figure 9) experiences a significant increase. Meanwhile, compared with the results in the PE-base case, the radial component exhibits a larger decrease in the region near the impeller tip (i.e. for $z/H = 0.33$). This latter behavior leads to a larger reduction in the radial fluctuation as seen in Figure 6. At $2r/D_\mathrm{t} = 0.80$ (Figure 8), all three terms are suppressed by particles, but the combined reduction in the production and the convection surpasses that in the dissipation, causing both components of the fluctuation to decrease as seen in Figure 7.

3.2 Effects of operational parameters

This section discusses the effects of the operational parameters on the two-phase flow field. These comprise effects of the particle size, the mean solid fraction, and the impeller rotation speed. It turns out both in the simulations and in the experiment that only the liquid velocity fluctuation and the solid fraction are significantly affected by these parameters. These will therefore be the focus of the discussion in the following.

3.2.1 Particle size

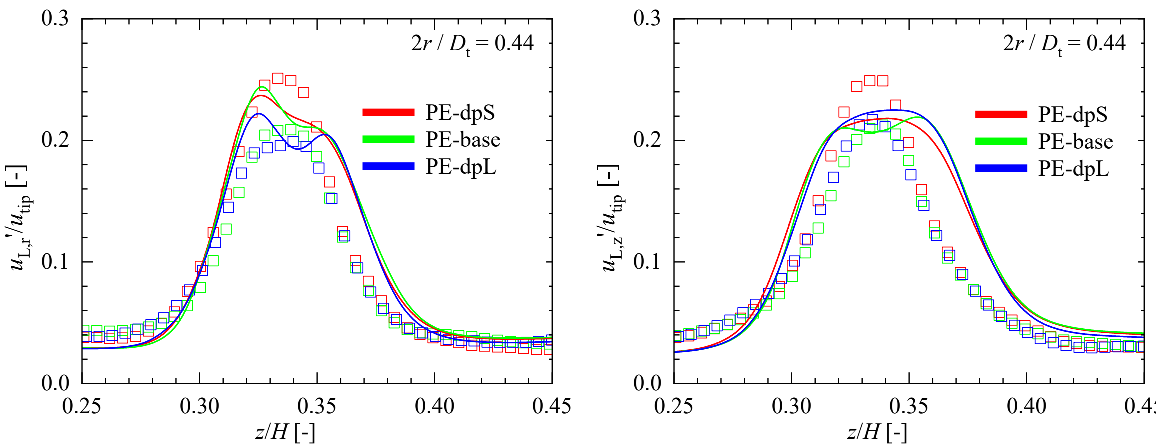

Figure 10. Axial profiles of the radial (left) and axial (right) components of liquid velocity fluctuation at a radial position $2r/D_\mathrm{t} = 0.44$ in cases with different sizes of PE particles. Lines: simulation results; symbols: experimental data from Sommer et al. (2021). Case details: Ω = 1500 rpm, ρ_S/ρ_L = 1.1, and $\bar{\alpha}_{S,\mathrm{ave}}$ = 0.05% in all cases; the particle diameters are 0.067 mm, 0.165 mm, and 0.425 mm in the dpS, base, and dpL cases, respectively.

For both the PE and the GL particles, three different sizes with $d_\mathrm{p} = 0.067, 0.165$, and ~ 0.425 mm are considered. The corresponding results are denoted as “dpS”, “base”, and “dpL”, respectively. Concerning the liquid velocity fluctuation, it is revealed both by the computations and by the experiment that more pronounced size effects occur for the PE than for the GL particles. Therefore, only the results involving PE particles will be discussed. Figure 10 summarizes the results for the radial and the axial components of the fluctuation at $2r/D_\mathrm{t} = 0.44$. Experimental results indicate a tendency of increasing peak for both the radial and axial fluctuations with decreasing particle size. Simulation results for the radial fluctuation qualitatively reproduce this tendency. For the predicted profiles of the axial fluctuation, however, no notable trend could be observed. This mismatch is likely due to the lack of PIT model in the present simulations and will be examined in more detail in section 3.3.

Figure 11 summarizes the results for the horizontally averaged solid fraction for PE (left panel) and GL (right panel) particles. Since experimental results were not provided for the smallest size (i.e. dpS), results are shown only for the two larger ones. With the particle size increasing from base to dpL, experimental results available in the axial portion away from the tank bottom (i.e. for $z/H > 0.2$) reveal a reduction in the averaged solid fraction, which is more pronounced for GL particles. Mass conservation yields that the solid fraction in the residual portion, i.e. the region close to the tank bottom, must be much higher than the mean value. This variation is confirmed by the simulations. In particular, for both particles, the predicted solid fraction for $z/H < 0.1$ in the two dpL cases is significantly larger than that in the two base cases. Compared with the experimental results, good agreement is achieved for PE particles of both sizes; for the larger GL particles, however, a significant underestimation takes place for $z/H > 0.3$.

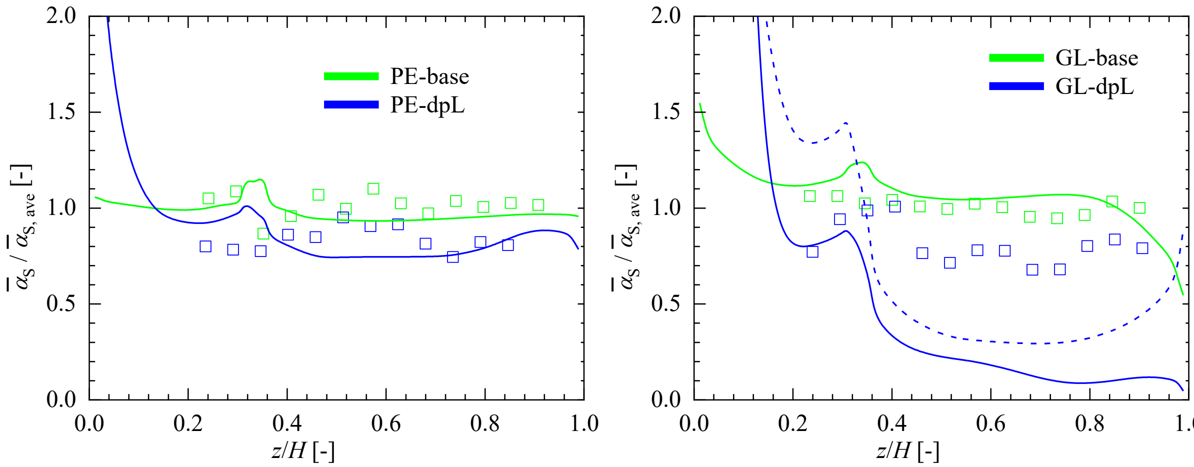

Figure 11. Results for the horizontally averaged volume fraction of PE (left, i.e. ρ_S/ρ_L = 1.1) and GL (right, i.e. ρ_S/ρ_L = 2.5) particles along the height of the tank in cases with different particle sizes. Solid (dashed) lines: simulation results from mesh 180 (240); symbols: experimental data from Sommer et al. (2021). Case details: Ω = 1500 rpm and $\bar{\alpha}_{S,\text{ave}}$ = 0.05% in all cases; the particle diameters are 0.165 mm and 0.425 mm in the base and dpL cases, respectively.

The deviation in the GL-dpL case might be due to the applied mesh, the resolution of which was found too low to reproduce the experimental results for the GL-base case near the top of the tank. To check this possibility, an additional run for the GL-dpL case based on mesh 240 (see section B of the Supplementary Material for details) is conducted. The corresponding prediction appears in the right panel of Figure 11 as a dashed line. Comparing the two blue lines reveals a moderate increase in the solid fraction in the region above the impeller with increasing mesh resolution. Moreover, the difference in the results from the two meshes is more pronounced than that revealed in the GL-base case (see Figure 4), indicating that the resolution of mesh 240 might be still insufficient for the GL-dpL case. Assessment of meshes beyond mesh 240, however, is unaffordable based on the available computational resources.

3.2.2 Mean solid fraction

Three different mean solid fractions with $\bar{\alpha}_{S,\text{ave}} = 0.025\%, 0.05\%$, and 0.1% are considered for both the PE and the GL particles. The corresponding results are denoted by “vof”, “base”, and “vofL”, respectively.

Figure 12 shows some of the typical results for the liquid velocity fluctuation obtained at a radial position $2r/D_\mathrm{t} = 0.44$. Only results for the radial fluctuation are presented as those for the axial ones show similar features. In view of the experiment, it is seen that the presence of PE particles (left panel) tends to decrease the liquid fluctuation in particular when the solids loading is low. As for the GL results (right panel), a moderate increase in the liquid fluctuation with increasing mean solid fraction can be observed. These observations are well reproduced by the simulations.

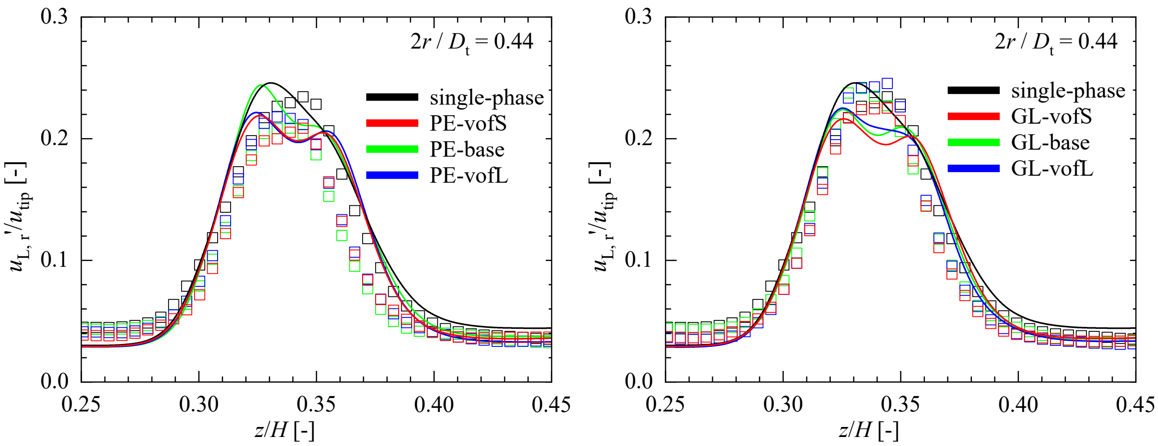

Figure 12. Axial profiles of the radial fluctuation at a radial position $2r/D_\mathrm{t} = 0.44$ in cases with different loading of PE (left, i.e. ρ_S/ρ_L = 1.1) and GL (right, i.e. ρ_S/ρ_L = 2.5) particles. Lines: simulation results; symbols: experimental data from Sommer et al. (2021). Case details: Ω = 1500 rpm and d_p = 0.165 mm in all cases; the mean solid volume fractions are 0.025%, 0.05%, and 0.1% in the vofS, base, and vofL cases, respectively.

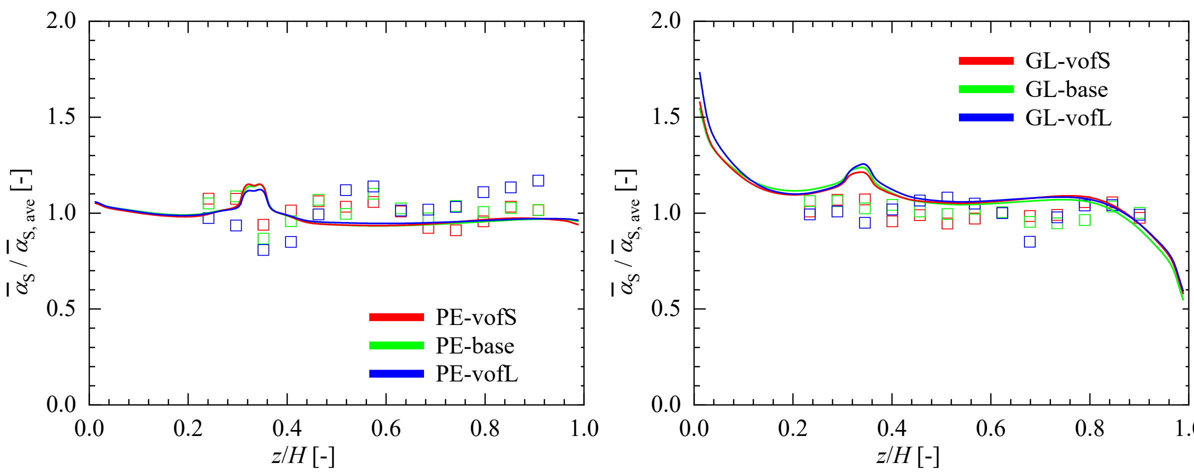

Figure 13. Results for the horizontally averaged volume fraction of PE (left) and GL (right) particles along the height of the tank in cases with different loading of particles. Lines, symols, and case details as in Figure 12.

Figure 13 summarizes the results for the horizontally averaged solid fraction along the height of the tank. Experimental results show no definite trend in the normalized value with increasing mean solid fraction; the relatively scattered results in the two cases with highest solid loading are likely a consequence of the experimental uncertainty. Simulation results also show a vanishingly small effect of the mean solid fraction and achieve quite good quantitative agreement with the experimental results.

3.2.3 Impeller rotation speed

Three different impeller rotation speeds of $\Omega = 650, 1000$, and 1500 rpm are considered. Only cases with PE particles are simulated, as in the corresponding cases with GL particles no complete suspension could be achieved at the lower two impeller rotation speeds in the experiment. The results obtained at these three different impeller rotation speeds are denoted by "rpm650", "rpm1000", and "base", respectively.

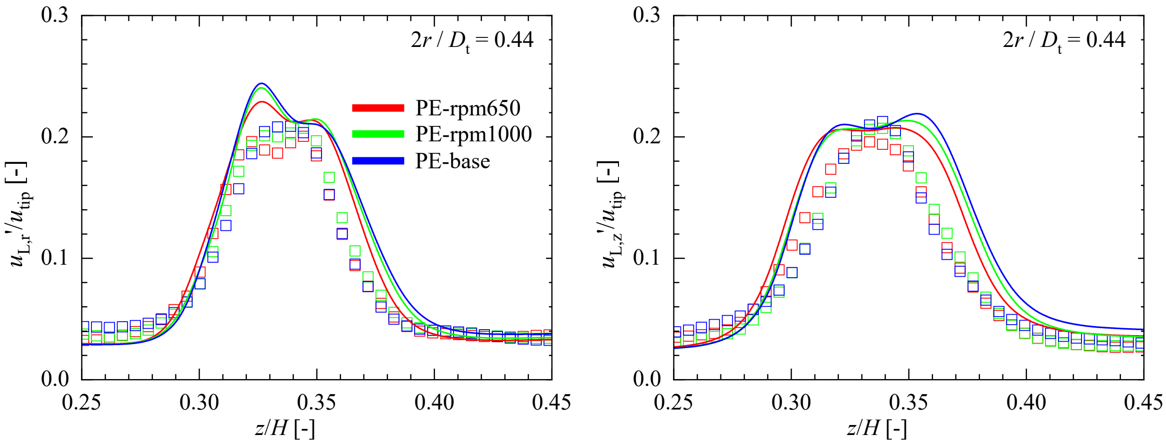

Figure 14. Axial profiles of the radial (left) and axial (right) components of the liquid velocity fluctuation in the three PE-laden cases, i.e. $\rho_S/\rho_L = 1.1$, with different impeller rotation speeds at a radial position $2r/D_t = 0.44$. Lines: simulation results; symbols: experimental data from Sommer et al. (2021). Case details: $d_p = 0.165$ mm and $\bar{\alpha}_{S,\mathrm{ave}} = 0.05\%$ in all cases; the impeller rotation speeds are 650 rpm, 1000 rpm, and 1500 rpm in the rpm650, rpm1000, and base cases, respectively.

Results for the liquid velocity fluctuation at a radial position $2r/D_t = 0.44$ are summarized in Figure 14. Experimental results indicate that, when normalized by the corresponding impeller tip velocity, the peaks of both the radial (left panel) and the axial (right panel) components of velocity fluctuation show a tiny decrease with decreasing impeller rotation speed, which is qualitatively reproduced by the simulations.

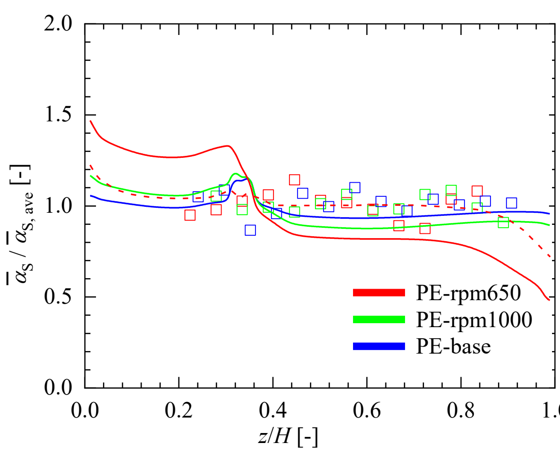

Figure 15. Results for the horizontally averaged volume fraction of PE particles along the height of the tank in cases with different impeller rotation speeds. Lines, symols, and case details as Figure 14.

Figure 15 compares the results for the horizontally averaged solid fraction obtained at the three different impeller rotation speeds. The experiment shows no definite trend in the results obtained at all three impeller rotation speeds, indicating that the flow is already in the fully suspended state at the lowest impeller rotation speed (i.e. at $\Omega = 650$ rpm). Similarly, simulation results obtained at the larger two impeller rotation speeds show only slight deviation; their agreement with the corresponding experimental results is also as expected. At the lowest impeller rotation speed, however, simulation results differ from the experiment. In particular, the predicted solid fraction in the region beneath the impeller is approximately 30% higher than the mean value, leading to a moderate underestimation of the experimental results in the region above the impeller. This mismatch may be a consequence of insufficient mesh resolution, which has been shown to cause similar deviation for GL particles (Figure 11). This is confirmed by the results of an additional run using mesh 240 (dashed line in the right panel of Figure 15), according to which the flow at $\Omega =$ 650 rpm is in the fully suspended state, in agreement with the corresponding experimental results.

3.3 Performance of available PIT models

Experimental results shown in the last two sections revealed notable turbulence modulation by the particles. Although no PIT model has been employed, the simulation results are capable to qualitatively reproduce the particle effects. To improve quantitative predictions, however, the PIT should be taken into account as well. This is feasible by combining the closure models outlined in section 2.1 with the PIT models summarized in section 2.2. Following this methodology, the performance of the various PIT models is assessed in this section. To reduce the computational effort, three typical cases are considered, namely PE-base, GL-base, and PE-dpS-vofL (see Table 2 for the case details), in which the liquid fluctuations were observed in the experiment to be suppressed, unaffected, and augmented.

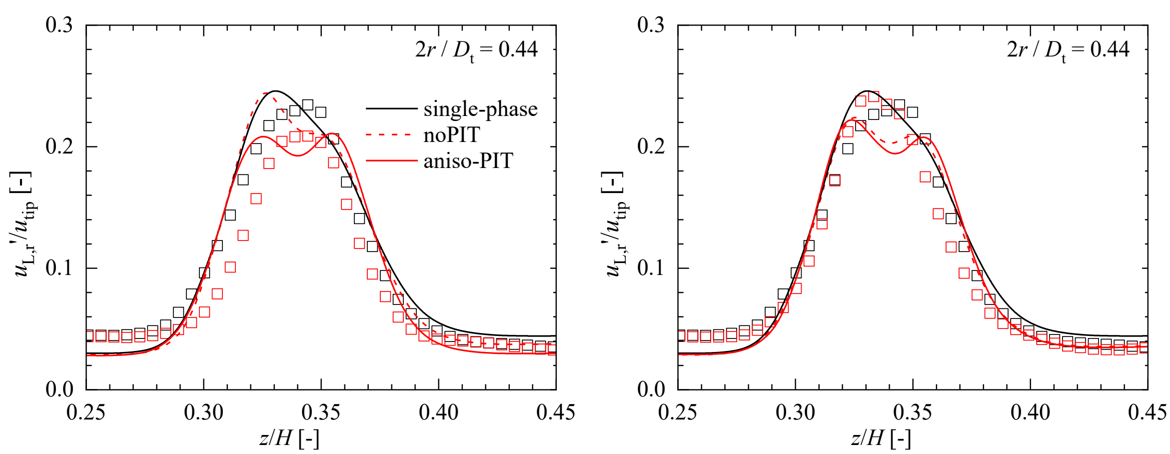

Figure 16. Axial profile of the radial component of the liquid velocity fluctuation at a radial position $2r/D_t = 0.44$. Black symbols (line) denote the experimental (computational) results in the single-phase case. Red symbols (lines) in the left and right panels correspond to the experimental (computational) results in the PE-base and GL-base cases, respectively.

The aniso-PIT model is assessed first, as it represents the best currently available description. The predictions are compared with those obtained without adopting any PIT model (denoted as "noPIT") to gain an idea on the performance of this model. Figure 16 provides some of the typical results for the radial component of the liquid velocity fluctuation obtained for the two base cases. In the case PE-base (left panel), the prediction without the PIT model shows only a slight turbulence suppression (comparing the red dashed line with the black solid line), while moderate turbulence suppression is seen in the experiment. This mismatch is eliminated by adopting the anisotropic PIT model. In particular, the sizable reduction in the peak of the fluctuation is more satisfactorily reproduced. In the case with GL particles, both predictions show a moderate decrease in the peak, and virtually no difference between the two predictions can be observed; in the experiment, however, hardly any turbulence modulation by GL particles can be observed.

The weak turbulence modulation revealed in the GL-base case is a bit surprising, although this is also confirmed by the experiment. Since the inertia of GL particles is greater, the resulting turbulence modulation is expected to be stronger than that by PE particles. To further clarify why this is not observed, the difference between the budgets of the turbulent kinetic energy, based on Eq. (3), obtained with and without the addition of the anisotropic PIT model is examined. The production ($0.5P_{ii}$), dissipation ($-\varepsilon$), mean-flow convection ($-\mathrm{D}k/\mathrm{D}t$), and PIT-source ($S^k/\alpha_L\rho_L$) obtained in the two base cases are shown in Figure 17. For both cases, the source by PIT is vanishingly small compared with the other terms. In addition, it can be observed that virtually no change in the dissipation is caused by the anisotropic PIT model. In the production term in contrast, it causes a notable reduction, which is more pronounced for PE particles. This reduction is only partially compensated by the increase in the mean-flow convection, leading to a reduction in the liquid velocity fluctuation in particular in the PE-base case as seen in Figure 16.

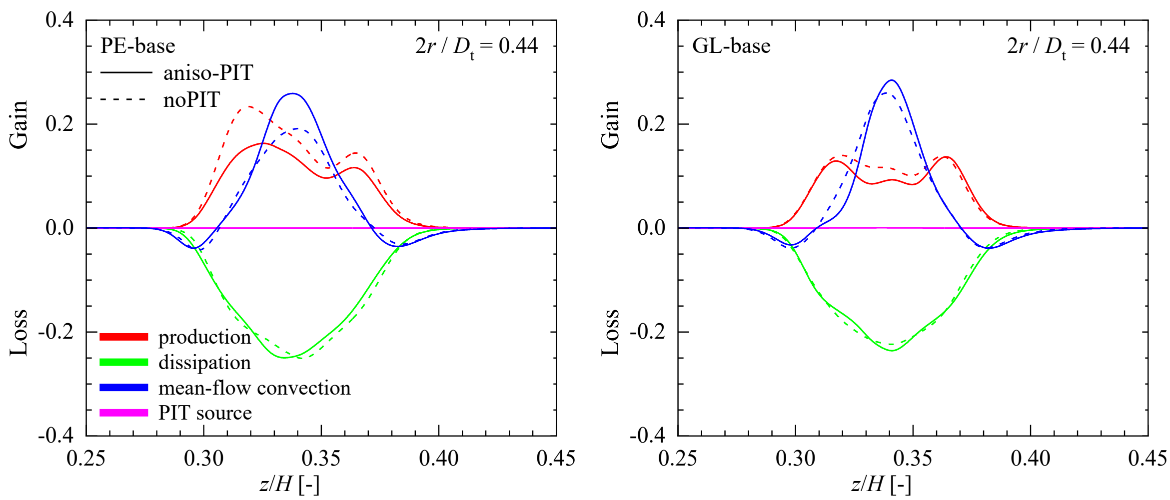

Figure 17. Simulation results for the turbulent-kinetic-energy budget in the two cases of PE-base (left) and GL-base (right) at a radial position $2r/D_\mathrm{t} = 0.44$. Different colors denote different terms as detailed in the left panel. All quantities are normalized by $u_\mathrm{tip}^3/D_\mathrm{t}$.

The assessment proceeds by considering the case PE-dpS-vofL, in which the liquid is loaded with PE particles with a diameter of ~ 0.067 mm and a volume fraction of 0.1%. All three different PIT models introduced in section 2.2, i.e. aniso-PIT, iso-PIT, and Sato-PIT, are tested. Figure 18 compares the predictions for the liquid velocity fluctuation with the experimental results at $2r/D_\mathrm{t} = 0.44$. The measured peaks of both the radial and axial components of the fluctuation are seen to be approximately 50% larger than their counterparts in the single-phase case (black symbols in Figure 16). This augmentation is not reproduced by any of the simulations. Rather, comparing the simulation results with those in the single-phase case (black lines in Figure 16) reveals a turbulence suppression by the particles. This suppression is seen to be more pronounced in the radial component in simulations with PIT models, i.e. the prediction is deteriorated by all PIT models.

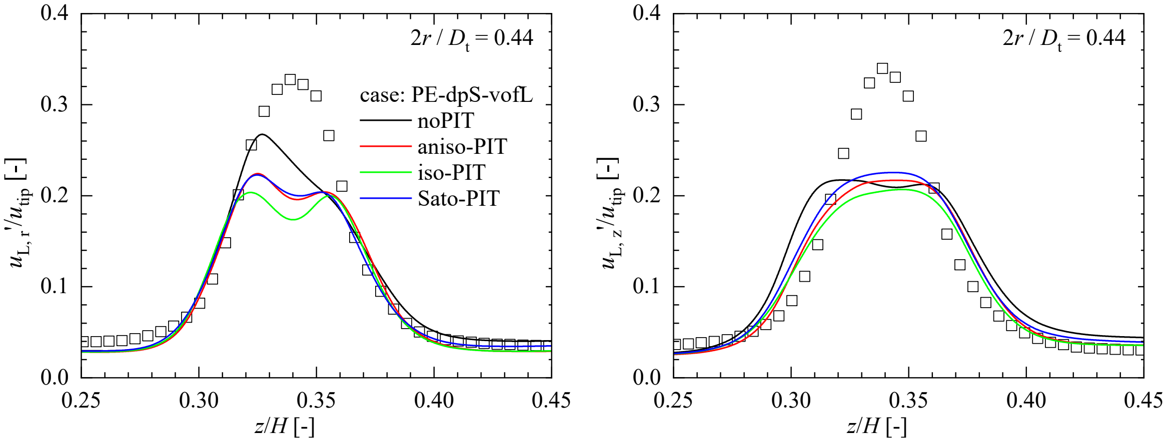

Figure 18. Axial profiles of the radial (left) and axial (right) components of the liquid velocity fluctuation in the case PE-dpS-vofL at a radial position $2r/D_t = 0.44$. Lines: simulation results by different models distinguished by colors; symbols: experimental data from Sommer et al. (2021). Case details: Ω = 1500 rpm, ρ_S/ρ_L = 1.1, $\bar{\alpha}_{S,\mathrm{ave}}$ = 0.1%, $d_p \approx$ 0.067 mm.

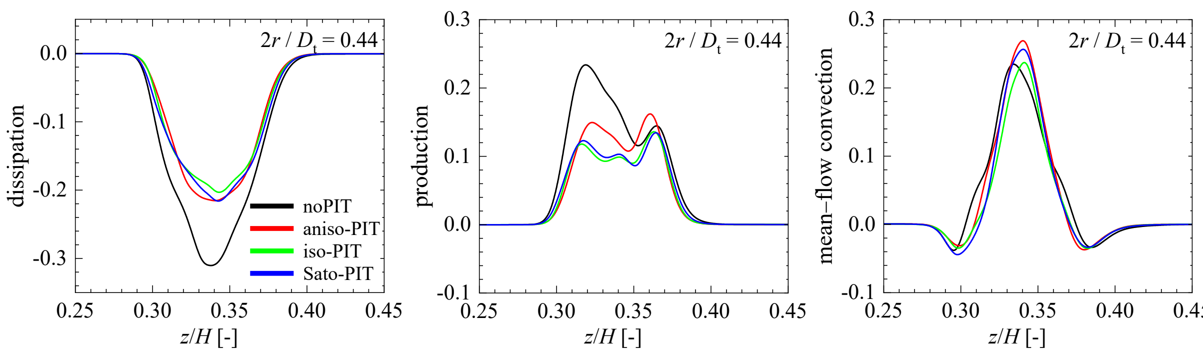

Figure 19. Simulation results for the turbulent-kinetic-energy budget in the case PE-dpS-vofL at a radial position $2r/D_t = 0.44$. Left: dissipation; middle: production; right: mean-flow convection. All quantities are normalized by u_{tip}^3/D_t.

To figure out the cause of this deterioration, again the budget of the turbulent kinetic energy is examined. Figure 19 presents the simulation results for the dissipation (left panel), the production (middle panel), and the mean-flow convection (right panel). Results for the PIT-source obtained in the two simulations applying the anisotropic (aniso-PIT) and the isotropic (iso-PIT) models, respectively, are not shown, as their magnitudes are again vanishingly small compared with the three terms above.

Concerning the dissipation, its magnitude is seen to be smaller in all simulations taking into account the PIT effects than that obtained in the simulation without PIT. This is encouraging as turbulence augmentation could be anticipated if all the other terms in the budget equation remained unchanged. However, as revealed in the middle and right panels of Figure 19, this is the case only for the mean-flow convection. For the production all models taking into account the PIT effects exhibit a significant reduction. Given that the PIT-source term is vanishingly small, this reduction causes a suppression of the calculated liquid fluctuation for all of these models. Close inspection of the two results applying the anisotropic and the isotropic PIT models indicates a more pronounced reduction in the dissipation in the iso-PIT results. However, the gain by the production is higher in the aniso-PIT results, which overcompensates the extra loss by the anisotropic model. This explains the slightly larger fluctuation obtained using the anisotropic PIT model than that using the isotropic one.

4 SUMMARY AND CONCLUSIONS

This work is dedicated to a comprehensive validation of the set of closure models assembled in Shi and Rzehak (2020), which comprise expressions for the interfacial forces including the drag, lift, and turbulent dispersion. Based on the Euler-Euler / RANS approach, these closure models were applied to predict the solid-liquid two-phase flows in a standard stirred tank reactor. To assess the performance of the set of closure models, the predictions were compared with a recent experiment by Sommer et al. (2021), in which spatially resolved data for the solid velocity and volume fraction as well as liquid velocity and turbulence were provided. The comparison concerned 14 different cases with variation in particle size, particle-to-liquid density ratio, mean solid volume fraction, and impeller rotation speed. It turns out that by and large the experimental data were reasonably well reproduced. However, the measurements show a small but clear effect of modulation of the liquid phase turbulence by the particles, which could not be captured by the simulations even with the aid of several particle-induced turbulence (PIT) models taken from the available literature.

Based on the present work and the previous ones from Shi and Rzehak (2018, 2020), several aspects that deserve further consideration can be identified as follows. First, the overestimation of the peak radial velocity in the single-phase case (Figure 1 and Figure 2, see also Fig. 6 in Sommer et al. 2021) by the SSG RSM model is a bit surprising, as very good agreement was obtained at comparable impeller Reynolds number in our previous work (Figs. 8 & 9 in Shi and Rzehak 2018, Fig. 4 in Shi and Rzehak 2020). The key difference among these cases lies in the magnitude of the typical shear rate. In the present work a very high impeller rotation speed (1500 rpm) was considered, making the typical shear rate involved much larger than those in the previous work. A possible reason relates to the no-slip boundary condition applied at the edge of the impeller, as there are evidences for the slip of Newtonian liquids at solid interfaces at high shear rates (Neto et al. 2005).

Second, an appropriate PIT model reproducing the turbulence modulation in solid-liquid stirred tank flows is still missing. In particular, neither the enhanced-eddy-viscosity model by Sato et al. (1981) nor the two source-term based models originating from Kataoka et al. (1992) were found capable to reproduce the turbulence enhancement revealed by the experiment in the case PE-dpS-vofL. For future model development, the most promising candidate is likely the latter approach, as it allows to directly modify the turbulent kinetic energy (or Reynolds stress) and the dissipation using appropriate source terms. The still open question here is the lack of general expressions that are capable of accurately describing the variation in these source terms over a broad range of parameters.

Furthermore, the mismatch between the predicted turbulence modulation using the source-term based PIT models and the experimental data deserves some further discussion. The source for the turbulent kinetic energy is always treated as proportional to the work by the drag. In the present work, the magnitude of the PIT source following this estimation was found always vanishingly small, owing to the small slip velocity (therefore small slip Reynolds number). Therefore, we expect that new proposals for the source term in the dissipation equation have to be established and assessed. More specifically, in the present work the source for turbulence dissipation is treated as proportional to the drag coefficient [first part of Eq. (10)] which depends on the slip Reynolds number only. This treatment is certainly not general since other aspects, like e.g. the finite-size effects (Yeo et al. 2010) and the effects of particle inertia (Ferrante and Elghobashi 2003), which are known to be responsible for the modulation of the dissipation over a certain range of parameters, are not accounted for. In this context, it seems promising to propose a more general expression by relating the dissipation source with the particle momentum number (Tanaka and Eaton 2008).

Moreover, the choice for the timescale relating the two distinct source terms has to be revisited. The reasonability of the timescale used in the present work, $\tau = d_{\mathrm{p}}/u_{\mathrm{rel}}$, has been justified only for flows with large slip Reynolds numbers [$Re_{\mathrm{p}} = O(100)$, Ma et al. (2017)]. A key feature of such flows is that the turbulence modulation is largely governed by the wake dynamics. For flows with low-to-moderate Re_{p} as considered in the present work, the wake is weak and there is no guarantee that the same choice for the timescale still applies. Further assessment using other possible timescale candidates (Rzehak and Krepper 2013) may be necessary. Recent DNS studies on turbulence modulation (e.g. Yu et al. 2021, Xia et al. 2021) may provide a sufficient data source to make progress in this direction.

Third, knowledge on the required mesh resolution is insufficient. Prior work addressing this numerical issue mainly concerned the flow in the single-phase case (e.g. Coroneo et al. 2011, Lane 2017), while the requirement of a relatively higher mesh resolution in the corresponding two-phase cases is revealed comparing the preliminary results reported in this work and those in Sommer et al. (2021). This is particularly important in obtaining mesh independent results for the particle distribution. The present work indicated that higher mesh resolution is required in cases with larger particle size, larger particle density, and smaller impeller rotation speed. Whether these are general trends needs further check.

Finally yet importantly, the development of reliable CFD models should be accompanied by the acquisition of more accurate and more comprehensive data for validation. Further experimental data and highly-resolved simulation results on wider operational conditions would be desirable such as higher solid fraction, partially suspended conditions and maybe some more challenging situations with polydisperse particles and non-standard tank geometries.

5 ACKNOWLEDGEMENT

This project has received funding from the European Union's Horizon 2020 research and innovation program FineFuture under Grant Agreement No 821265. Computational resources were provided by HZDR.

6 REFERENCES

Balachandar, S. and Eaton, J.K., 2010. Turbulent dispersed multiphase flow. *Annual Review of Fluid Mechanics* 42, 111–133.

Bujalski, W., Nienow, A., Chatwin, S., Cooke, M., 1986. The dependency on scale and material thickness of power number of different impeller types. *Proceedings of the International Conference on Mechanical Agitation*, p. 37.

Chapple, D., Kresta, S.M., Wall, A. and Afacan, A., 2002. The effect of impeller and tank geometry on power number for a pitched blade turbine. *Chemical Engineering Research and Design* 80, 364–372.

Chen, Y., Jiang, H. and Huang, X., 2011. Turbulence Properties of Solid-liquid Flow in the Near Wall Region of Stirred Tank. *Journal of Chemical Engineering of Japan* 44, 224–232.

Colombo, M. and Fairweather, M., 2015. Multiphase turbulence in bubbly flows: RANS simulations. *International Journal of Multiphase Flow* 77, 222–243.

Coroneo, M., Montante, G., Paglianti, A. and Magelli, F., 2011. CFD prediction of fluid flow and mixing in stirred tanks: Numerical issues about the RANS simulations. *Computers & Chemical Engineering* 35, 1959–1968.

Lopez de Bertodano, M.A.L., 1998. Two fluid model for two-phase turbulent jets. *Nuclear Engineering and Design* 179, 65–74.

Deen, N.G., Solberg, T. and Hjertager, B.H., 2002. Flow generated by an aerated Rushton impeller: two-phase PIV experiments and numerical simulations. *The Canadian Journal of Chemical Engineering* 80, 1–15.

Derksen, J.J., 2003. Numerical simulation of solids suspension in a stirred tank. *AIChE Journal* 49, 2700–2714.

Derksen, J.J., 2018. Eulerian-Lagrangian simulations of settling and agitated dense solid-liquid suspensions–achieving grid convergence. *AIChE Journal* 64, 1147–1158.

Drew, D.A. and Passman, S.L., 2006. Theory of multicomponent fluids. S*pringer Science & Business Media*.

Druzhinin, O.A. and Elghobashi, S., 1999. On the decay rate of isotropic turbulence laden with microparticles. *Physics of Fluids* 11, 602–610.

Eaton, J.K., 2009. Two-way coupled turbulence simulations of gas-particle flows using point-particle tracking. *International Journal of Multiphase Flow* 35, 792–800.

Eaton, J.K. and Fessler, J., 1994. Preferential concentration of particles by turbulence. *International Journal of Multiphase Flow* 20, 169–209.

Elgobashi, S., 2006. An updated classification map of particle-laden turbulent flows. *In IUTAM Symposium on Computational Approaches to Multiphase Flow*, 3–10. Springer, Dordrecht.

Elghobashi, S. and Truesdell, G., 1993. On the two - way interaction between homogeneous turbulence and dispersed solid particles. I: Turbulence modification. *Physics of Fluids A: Fluid Dynamics* 5, 1790–1801.

Feng, X., Li, X., Cheng, J., Yang, C. and Mao, Z.S., 2012. Numerical simulation of solid–liquid turbulent flow in a stirred tank with a two-phase explicit algebraic stress model. *Chemical Engineering Science* 82, 272–284.

Ferrante, A. and Elghobashi, S., 2003. On the physical mechanisms of two-way coupling in particle-laden isotropic turbulence. *Physics of Fluids*, 15, 315–329.

Gabriele, A., Tsoligkas, A.N., Kings, I.N. and Simmons, M.J.H., 2011. Use of PIV to measure turbulence modulation in a high throughput stirred vessel with the addition of high Stokes number particles for both up-and down-pumping configurations. *Chemical Engineering Science* 66, 5862–5874.

Gai, G., Hadjadj, A., Kudriakov, S. and Thomine, O., 2020. Particles-induced turbulence: A critical review of physical concepts, numerical modelings and experimental investigations. *Theoretical and Applied Mechanics Letters* 10, 241–248.

Geiss, S., Dreizler, A., Stojanovic, Z., Chrigui, M., Sadiki, A. and Janicka, J., 2004. Investigation of turbulence modification in a non-reactive two-phase flow. *Experiments in Fluids* 36, 344–354.

Gillissen, J.J.J. and Van den Akker, H.E.A., 2012. Direct numerical simulation of the turbulent flow in a baffled tank driven by a Rushton turbine. *AIChE Journal* 58, 3878–3890.

Guha, D., Ramachandran, P.A., Dudukovic, M.P. and Derksen, J.J., 2008. Evaluation of large Eddy simulation and Euler-Euler CFD models for solids flow dynamics in a stirred tank reactor. *AIChE Journal* 54, 766–778.

Gore, R.A. and Crowe, C.T., 1989. Effect of particle size on modulating turbulent intensity. *International Journal of Multiphase Flow* 15, 279–285.

Hetsroni, G., 1989. Particles-turbulence interaction. *International Journal of Multiphase Flow* 15, 735–746.

Hoque, M.M., Mitra, S., Sathe, M.J., Joshi, J.B. and Evans, G.M., 2016. Experimental investigation on modulation of homogeneous and isotropic turbulence in the presence of single particle using time-resolved PIV. *Chemical Engineering Science* 153, 308–329.

Hosokawa, S. and Tomiyama, A., 2004. Turbulence modification in gas–liquid and solid–liquid dispersed two-phase pipe flows. *International Journal of Heat and Fluid Flow* 25, 489–498.

Kataoka, I., Besnard, D.C. and Serizawa, A., 1992. Basic equation of turbulence and modeling of interfacial transfer terms in gas-liquid two-phase flow. *Chemical Engineering Communications* 118, 221–236.

Kim, S.D. and Kang, Y., 1997. Heat and mass transfer in three-phase fluidized-bed reactors—an overview. *Chemical Engineering Science* 52, 3639–3660.

Lane, G.L., 2017. Improving the accuracy of CFD predictions of turbulence in a tank stirred by a hydrofoil impeller. *Chemical Engineering Science 169*, 188–211.

Li, G., Li, Z., Gao, Z., Wang, J., Bao, Y. and Derksen, J.J., 2018. Particle image velocimetry experiments and direct numerical simulations of solids suspension in transitional stirred tank flow. *Chemical Engineering Science* 191, 288–299.

Lu, J., Peters, E.A.J.F. and Kuipers, J.A.M., 2019. Direct numerical simulation of fluid flow and dependently coupled heat and mass transfer in fluid-particle systems. *Chemical Engineering Science* 204, 203–219.

Ma, T., Santarelli, C., Ziegenhein, T., Lucas, D. and Fröhlich, J., 2017. Direct numerical simulation–based Reynolds-averaged closure for bubble-induced turbulence. *Physical Review Fluids* 2, 034301.

Ma, T., Lucas, D., Jakirlić, S., and Fröhlich, J., 2020. Progress in the second-moment closure for bubbly flow based on direct numerical simulation data. *Journal of Fluid Mechanics* 883, A9.

Mathai, V., Lohse, D. and Sun, C., 2020. Bubbly and buoyant particle–laden turbulent flows. *Annual Review of Condensed Matter Physics* 11, 529–559.

Mesa, D. and Brito-Parada, P.R., 2019. Scale-up in froth flotation: A state-of-the-art review. *Separation and Purification Technology* 210, 950–962.

Meyer, D.W., 2012. Modelling of turbulence modulation in particle-or droplet-laden flows. *Journal of Fluid Mechanics 706*, 251–273.

Mishra, P. and Ein-Mozaffari, F., 2020. Critical review of different aspects of liquid-solid mixing operations. *Reviews in Chemical Engineering* 36, 555–592.

Montante, G., Paglianti, A. and Magelli, F., 2012. Analysis of dilute solid–liquid suspensions in turbulent stirred tanks. *Chemical Engineering Research and Design* 90, 1448–1456.

Murthy, B.N., Kasundra, R.B. and Joshi, J.B., 2008. Hollow self-inducing impellers for gas–liquid–solid dispersion: Experimental and computational study. *Chemical Engineering Journal* 141, 332–345.

Neto, C., Evans, D.R., Bonaccurso, E., Butt, H.J. and Craig, V.S., 2005. Boundary slip in Newtonian liquids: a review of experimental studies. *Reports on Progress in Physics* 68, 2859.

Nouri, J.M. and Whitelaw, J.H., 1992. Particle velocity characteristics of dilute to moderately dense suspension flows in stirred reactors. *International Journal of Multiphase Flow* 18, 21–33.

Ochieng, A. and Onyango, M.S., 2008. Drag models, solids concentration and velocity distribution in a stirred tank. *Powder Technology* 181, 1–8.

Parekh, J. and Rzehak, R., 2018. Euler-Euler multiphase CFD-simulation with full Reynolds stress model and anisotropic bubble-induced turbulence. *International Journal of Multiphase Flow* 99, 231–245.

Poelma, C., Westerweel, J. and Ooms, G., 2007. Particle–fluid interactions in grid-generated turbulence. *Journal of Fluid Mechanics 589*, 315–351.

Qi, N., Zhang, H., Zhang, K., Xu, G. and Yang, Y., 2013. CFD simulation of particle suspension in a stirred tank. *Particuology* 11, 317–326.

Risso, F., Roig, V., Amoura, Z., Riboux, G. and Billet, A.M., 2008. Wake attenuation in large Reynolds number dispersed two-phase flows. *Philosophical Transactions of the Royal Society A: Mathematical, Physical and Engineering Sciences* 366, 2177–2190.

Rushton, J.H., Costich, E.W. and Everett, H.J., 1950. Power characteristic of mixing impellers. Part II. *Chemical Engineering Progress* 46, 457–476.

Rutherford, K., Mahmoudi, S.M., Lee, K.C. and Yianneskis, M., 1996. The influence of Rushton impeller blade and disk thickness on the mixing characteristics of stirred vessels. *Chemical Engineering Research & Design* 74, 369–378.

Rzehak, R. and Krepper, E., 2013. CFD modeling of bubble-induced turbulence. *International Journal of Multiphase Flow* 55, 138–155.

Santarelli, C. and Fröhlich, J., 2015. Direct numerical simulations of spherical bubbles in vertical turbulent channel flow. *International Journal of Multiphase Flow* 75, 174–193.

Santarelli, C. and Fröhlich, J., 2016. Direct numerical simulations of spherical bubbles in vertical turbulent channel flow. Influence of bubble size and bidispersity. *International Journal of Multiphase Flow* 81, 27–45.

Sato, Y., Sadatomi, M. and Sekoguchi, K., 1981. Momentum and heat transfer in two-phase bubble flow—I. Theory. *International Journal of Multiphase Flow* 7, 167–177.

Schiller, L. and Naumann, A., 1933. Fundamental calculations in gravitational processing. *Zeitschrift Des Vereines Deutscher Ingenieure* 77, 318–320.

Schwarz, M.P., Koh, P.T.L., Wu, J., Nguyen, B. and Zhu, Y., 2019. Modelling and measurement of multi-phase hydrodynamics in the Outotec flotation cell. *Minerals Engineering* 144, 106033.

Shan, X., Yu, G., Yang, C., Mao, Z.S. and Zhang, W., 2008. Numerical simulation of liquid− solid flow in an unbaffled stirred tank with a pitched-blade turbine downflow. *Industrial & Engineering Chemistry Research* 47, 2926–2940.

Shi, P. and Rzehak, R., 2018. Bubbly flow in stirred tanks: Euler-Euler/RANS modeling. *Chemical Engineering Science* 190, 419–435.

Shi, P. and Rzehak, R., 2019. Lift Forces on Solid Spherical Particles in Unbounded Flows. *Chemical Engineering Science* 208, 115145.

Shi, P. and Rzehak, R., 2020. Solid-liquid flow in stirred tanks: Euler-Euler/RANS modeling. *Chemical Engineering Science* 227, 115875.

Sommer, A.E., Rox, H., Shi, P., Eckert, K. and Rzehak, R., 2021. Solid-liquid flow in stirred tanks:“CFD-grade” experimental investigation. *Chemical Engineering Science* 245, 116743.

Speziale, C. G., Sarkar, S. and Gatski, T. B., 1991. Modeling the pressure–strain correlation of turbulence: an invariant dynamical systems approach, *Journal of Fluid Mechanics* 227, 245–272.

Tamburini, A., Cipollina, A., Micale, G. and Brucato, A., 2013. Particle distribution in dilute solid liquid unbaffled tanks via a novel laser sheet and image analysis based technique. *Chemical Engineering Science* 87, 341–358.

Tanaka, T. and Eaton, J.K., 2008. Classification of turbulence modification by dispersed spheres using a novel dimensionless number. *Physical Review Letters* 101, 114502.

Unadkat, H., Rielly, C.D., Hargrave, G.K. and Nagy, Z.K., 2009. Application of fluorescent PIV and digital image analysis to measure turbulence properties of solid–liquid stirred suspensions. *Chemical Engineering Research and Design* 87, 573–586.

Wang, F., Wang, W., Wang, Y. and Mao, Z., 2003. CFD simulation of solid-liquid two-phase flow in baffled stirred vessels with Rushton impellers. *Proceedings of the 3rd International Conference on CFD in the Minerals and Process Industries*, 287–292.

Wu, J., Wang, S., Nguyen, B., Lane, G., Graham, L., Short, G. and Rüster, J., 2015. Improved viscous slurry agitation for minerals processing. *Minerals Engineering* 78, 21–31.

Xia, Y., Lin, Z., Pan, D. and Yu, Z., 2021. Turbulence modulation by finite-size heavy particles in a downward turbulent channel flow. *Physics of Fluids* 33, 063321.

Yeo, K., Dong, S., Climent, E. and Maxey, M.R., 2010. Modulation of homogeneous turbulence seeded with finite size bubbles or particles. *International Journal of Multiphase Flow* 36, 221–233.

Yu, Z., Xia, Y., Guo, Y. and Lin, J., 2021. Modulation of turbulence intensity by heavy finite-size particles in upward channel flow. *Journal of Fluid Mechanics* 913.